DTU Physics
Department of Physics

Bachelor thesis

Theory and modeling of all-polymer based acoustofluidic devices

William N. Bodé s141209
Thor H. Snedker s136549

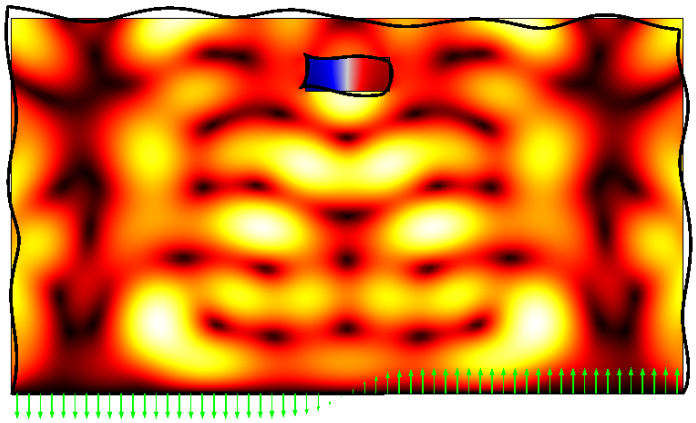

Supervisor: Prof. Henrik Bruus

Department of Physics
Technical University of Denmark

19 June 2017

Abstract

The applications of acoustofluidic devices has shown promising results using high acoustic impedance materials such as glass or Silicon, with regard to acoustophoresis. In this thesis we model and investigate all-polymer based acoustofluidic devices with particularly focus on PMMA, due to low costs and commercial availability. We present a 2D model constructed in the Finite Element Method (FEM) simulation software `COMSOL`, where we couple the dynamics of linear elastic solids with Newtonian fluids by imposing certain boundary conditions. We study four device candidates with different geometrical properties, by conducting an eigenfrequency search and evaluating the candidates by acoustic energies, half-wave resonances, acoustic forces and effective particle focusing times. Finally we compare our results with experiments conducted at Lund University in Sweden, as carried out by `AcouSort AB`, evaluated on the same parameters, to establish a connection between theory, simulations and experiments.

Preface

This thesis is submitted as fulfillment of the prerequisites for obtaining our Bachelor of Science degrees in Earth and Space Physics and Engineering (Thor) and Physics and Nanotechnology (William) from the Technical University of Denmark. We have conducted our work from which covers 15 ECTS-points each, from February 8th, 2017 to June 19th, 2017. The work has been carried out at Department of Physics in the Theoretical Microfluidics Group (TMF) with Professor Henrik Bruus as supervisor. We would like to thank the TMF group for providing a great work environment and for great cake and exciting discussions of different topics at the friday meetings. Thanks to Mikkel W.H. Ley for helping out when needed and also to Camilla Nyborg for reading and commenting our report.

Thor: First and foremost, I would like to give a deep and heartfelt thank to some very special people; our supervisor, professor Henrik Bruus, for giving me the great opportunity, honor and pleasure to write my Bachelor thesis under his competent supervision, for being a source of inspiration as a teacher and person in every way, for giving me several priceless new tools to acquire new knowledge and finally for being the best teacher I have ever had. My parents, Ellis and Ivan Heine Snedker, for unconditional support in every aspect of life, for challenging me to keep studying and for being the best and most loving family. William, last but not least, for being an amazing friend, a brilliant fellow student, an absolute crucial part of my time at DTU, and for the best teamwork one could imagine.

William: I want to thank Henrik for his incredible knowledge and sharing of this, throughout this project. One could not wish for a better supervisor and hopefully this is not the last time we will work together. Also a great applaus and thanks to Thor, who has been the partner i needed. Special thanks to my best friend and companion Nikoline, who always encourage me and lift my spirit, when it is needed! If it was not for her, i would not have managed my study.

Thor Heine Snedker
Department of Physics
Technical University of Denmark
19 June 2017

William Naundrup Bodé
Department of Physics
Technical University of Denmark
19 June 2017

Contents

List of Figures

List of Tables

List of symbols

Symbol	Description	Unit
N	Number of elements	
ε	Error value	
N_A	Avogadros constant	mol^{-1}
$\mathcal{M}$	Molar mass	$\mathrm{kg\,mol}^{-1}$
ρ	Mass density	$\mathrm{kg\,m}^{-3}$
p	Pressure	Pa
m	Particle mass	kg
$\boldsymbol{v}$	Velocity vector	$\mathrm{m\,s}^{-1}$
g	Generic field	
M	Mass	kg
Ω	Computational domain	
$\partial\Omega$	Domain boundary	
$\boldsymbol{J}$	Generic current vector	
$\boldsymbol{n}$	Outward surface normal vector	
$\boldsymbol{\sigma}$	Stress tensor	Pa
η	Dynamic viscosity	Pa s
β	Viscosity coefficient	
ν_k	Kinematic viscosity	$\mathrm{m\,s}^{-2}$
T	Temperature	K
k_B	Boltzmann constant	$\mathrm{m}^2\,\mathrm{kg\,s}^{-2}\,\mathrm{K}^{-1}$
n	Objects per unit volume	m^{-3}
R	Gas constant	$\mathrm{kg\,m}^2\,\mathrm{s}^{-2}\,\mathrm{K}^{-1}\,\mathrm{mol}^{-1}$
R_s	Specific gas constant ($R/\mathcal{M}$)	$\mathrm{m}^2\,\mathrm{s}^{-2}\,\mathrm{K}^{-1}$
C_V	Heat capacity	$\mathrm{Unit}(\mathrm{m}^2\,\mathrm{kg\,s}^{-2}\,\mathrm{K}^{-1}$
U	Internal energy	J
γ	Polytropic index	
c_0	Speed of sound	$\mathrm{m\,s}^{-1}$
k_0	Wavenumber	m^{-1}
Γ	Damping factor	

k	"Complex wavenumber"	m^{-1}
ω	Angular frequency	s^{-1}
κ	Compressiblity	Pa^{-1}
φ	Velocity potential	s^{-1}
E_{ac}	Acoustic energy density	$\mathrm{J\,m}^{-3}$
μ	Shear modulus	Pa
λ	Lamé's first parameter	Pa
$\boldsymbol{s}$	Strain tensor	
E	Young's modulus	Pa
$\dot{V}$	Volume flow rate	$\mathrm{m}^3\,\mathrm{s}^{-1}$
$\mathbb{N}_0$	Positive integers including zero	
$\mathbb{Z}$	All positive and negative integers	

Chapter 1

Concepts of a continuum

When analyzing kinematics and mechanical behavior of physical systems we naturally perceive matter as continuous, but as we know matter consists of molecules and inside these molecules we find particles which is surrounded by empty space, so in general matter are not continuous.

Dealing with continuum physics we say that matter is continuously distributed in space and fills out the entire region of interest, the bulk, and at the same time we can take an infinitesimal volume of the region having the same properties as the bulk. Saying that matter is continuously distributed is equivalent to a perfect resolution. In this thesis we shall treat solids and fluids as being continuous in space and time.

1.1 Matter

It is clear that the continuous description of matter does not hold for all length scales. Looking at atomic scales such as Ångstrøm we find that matter is quantized. Giving a quantitative estimate of the continuum length scale, starts with the assumption that molecular fluctuation inside a small volume V, inside a much larger region, obeys the Poisson distribution given in Eq. (A.1). With this probability distribution the variance is the number of molecules N which means that the relative error can be written as

$$\frac{\Delta N}{N} = \frac{\sqrt{N}}{N} = \frac{1}{\sqrt{N}} = \varepsilon. \tag{1.1}$$

Setting the relative error ε to 10^{-3} we can obtain a lower limit for the volume. For water we get

$$\frac{N}{V} = \frac{N_A}{\mathcal{M}_w}\rho_w = 33\,\mathrm{nm}^{-3} \tag{1.2}$$

molecules per unit volume, with molar mass $\mathcal{M}_w = 18\,\mathrm{g/mol}$ and $\rho_w = 1.0\,\mathrm{g/m}^3$ both for 1 atm and 20 °C. With the relative error 10^{-3} we write $N = \varepsilon^{-2}$, assuming that a single water molecule occupy a box with site length l we get

$$\frac{N}{V} = \frac{\varepsilon^{-2}}{l^3} = 33\,\mathrm{nm}^{-3}. \tag{1.3}$$

Under these conditions the length becomes $l = 31\,\mathrm{nm}$, which can be interpreted as a lower limit for which the continuum approximation holds within an error of 10^{-3}. This statistical approach is just one way of characterizing a length scale for which the continuum approximation holds, in reality it is much more complex. The Poisson distribution holds best for gases, but working with volumes consisting of $\sim 10^{21}$ molecules it is fair to say that the error goes like $\frac{\sqrt{N}}{N}$ and valid within an order of magnitude. It should also be mentioned that there exist an upper limit for which the continuum approximation is not valid, above this limit the properties of the bulk will differ.

1.2 Frame of reference

In general there are two ways of perceiving motion in fluids namely the Lagrangian and Eulerian picture. In Fig. 1.1 we follow a fluid parcel undergoing a flow as time passes. At time t we see that the velocity $\boldsymbol{v}$ of the fluid parcel is determined by the spacial components $\boldsymbol{r} = (x, y, z)$ inside the volume $\Delta V = \Delta x \Delta y \Delta z$, this is exactly the Eulerian frame of reference characterized by the control volume ΔV and the fixed frame of reference. One could on the other hand follow the fluid particle at any time meaning that the frame of reference is not fixed, this is the Lagrangian frame of reference. In the following we will use the Eulerian picture, which means that any field g in the fluid is determined by $g = g(\boldsymbol{r}, t)$, where g is generic in the sense that it can be both a scalar field or a vector field, so in general $g(\boldsymbol{r}, t)$ is a tensor field with rank zero up to two. It should also be emphasized that the field is described with respect to the parcels center of mass.

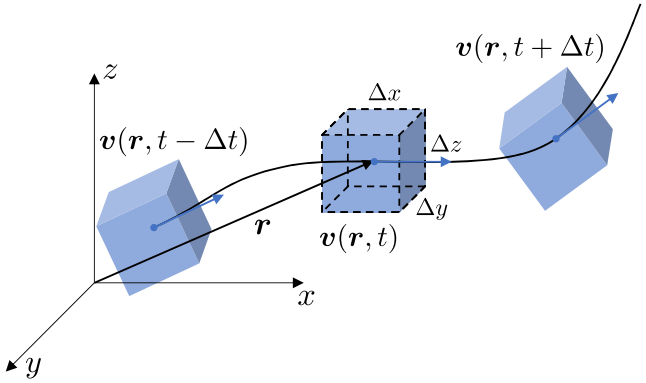

Figure 1.1: Reference frame showing the principles of the Eulerian way of perceiving fluid motions. The black line indicates the streamline for which the velocity is always tangent. The blue arrows indicates the velocity vector with respect to the center of mass at given time.

Within fluid mechanics it is natural to introduce both the density- and velocity field

$$\rho(\boldsymbol{r}, t) = \frac{1}{\Delta V} \sum_{i \in \Delta V} m_i \tag{1.4a}$$

$$\boldsymbol{v}(\boldsymbol{r}, t) = \frac{1}{\rho(\boldsymbol{r}, t) \Delta V} \sum_{i \in \Delta V} m_i \boldsymbol{p}_i, \tag{1.4b}$$

where the sum over the i'th element inside ΔV captures all fluid particles inside the control volume. Noting that the density is a scalar field where the velocity is a vector field. In general we can define a field, inside the fluid, as

$$\mathrm{d}G(\boldsymbol{r}, t) = g(\boldsymbol{r}, t)\mathrm{d}M = g(\boldsymbol{r}, t)\rho(\boldsymbol{r}, t)\mathrm{d}V \tag{1.5}$$

where we have made use of the continuum approximation saying that mass is continuously distributed inside V. The field $G(\boldsymbol{r}, t)$ is extrinsic in the sense that it scales with the system e.g. mass, where $g(\boldsymbol{r}, t)$ is intrinsic and does not scale with the system e.g. density. A concrete example of Eq. (1.5) could be $\mathrm{d}M = \rho(\boldsymbol{r}, t)\mathrm{d}V$.

In the following we will work with fluid dynamics, where the rate of change in the field is of interest,

$$\frac{\mathrm{d}g(\boldsymbol{r}, t)}{\mathrm{d}t} = \frac{\partial g}{\partial x}\frac{\mathrm{d}x}{\mathrm{d}t} + \frac{\partial g}{\partial y}\frac{\mathrm{d}y}{\mathrm{d}t} + \frac{\partial g}{\partial z}\frac{\mathrm{d}z}{\mathrm{d}t} + \frac{\partial g}{\partial t} = \frac{\partial g}{\partial t} + (\boldsymbol{v} \cdot \boldsymbol{\nabla})\, g, \tag{1.6}$$

which defines the operator

$$\frac{\mathrm{D}}{\mathrm{D}t} = \frac{\partial}{\partial t} + (\boldsymbol{v} \cdot \boldsymbol{\nabla})\,, \tag{1.7}$$

known as the material derivative, defined for every tensor field in the fluid, where $\boldsymbol{v}$ is the velocity of the fluid parcel. Working with infinitesimal volume elements we need to integrate over a given volume Ω, to describe global (extrinsic) values. In general the volume Ω can depend on time,

$$G(t) = \int_{\Omega(t)} g(\boldsymbol{r}, t)\rho(\boldsymbol{r}, t)\,\mathrm{d}V. \tag{1.8}$$

However in this thesis we will only consider steady volumes $\Omega(t) = \Omega$.

1.2.1 The pressure field

Pressure is a contact force acting on the surface of a body. In other words, pressure is a spatial scalar field acting on every point normal to the surface. Pressure acts towards the surface, and hence by convention of the unit normal vector, a minus sign appears on the surface normal $\boldsymbol{n}$. This pressure can be subdivided into numerous amounts of infinitesimal surface elements $\mathrm{d}\boldsymbol{A} = \boldsymbol{n}\mathrm{d}A$, that is, the normal to the surface of every surface-element $\mathrm{d}A$. The force exerted on the body, by the pressure field $p(\boldsymbol{r})$ then is,

$$\mathrm{d}\boldsymbol{F} = -p(\boldsymbol{r})\,\mathrm{d}\boldsymbol{A} \tag{1.9}$$

and the total force can then be obtained by integration over the entire surface, that is, adding all contributions from the surface elements

$$\boldsymbol{F} = -\oint_{\partial\Omega} p(\boldsymbol{r})\,\mathrm{d}\boldsymbol{A} = -\oint_{\partial\Omega} p(\boldsymbol{r})\boldsymbol{n}\,\mathrm{d}A. \tag{1.10}$$

This is the result for a pressure force acting with scalar pressure field $p(\boldsymbol{r})$ on a body of macroscopic size. Working with fluids on a microscopic scale, yields the need for exploration of pressure fields on a material particle. We utilize infinitesimal dimensions of a particle with volume $\mathrm{d}x\mathrm{d}y\mathrm{d}z = \mathrm{d}V$, experiencing pressure $p(\boldsymbol{r}) = p(x, y, z)$ in a fluid. The pressure on the side of this cube, is infinitesimally different,

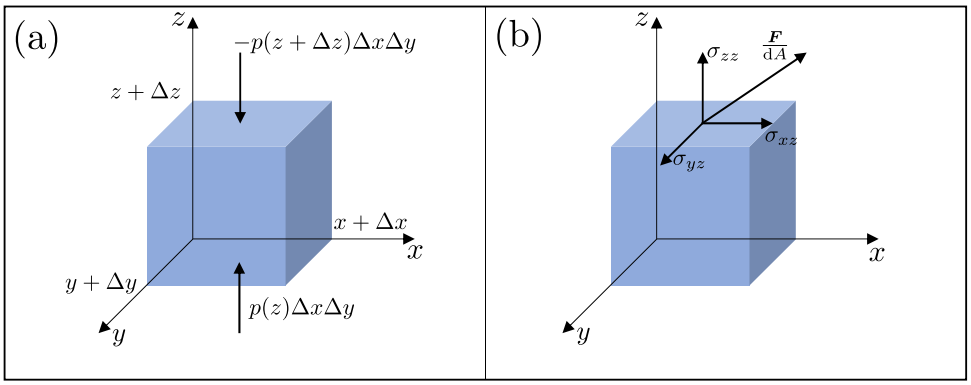

Figure 1.2: (a) Illustrating the concept of pressure on a material volume (blue). (b) Illustrating the general concept of stress on a infinitesimal material volume $\mathrm{d}V$ (blue).

$$\mathrm{d}F_z = [p(x,y,z) - p(x,y,z+\mathrm{d}z)]\,\mathrm{d}x\mathrm{d}y \approx -\partial_z p(\boldsymbol{r})\mathrm{d}x\mathrm{d}y\mathrm{d}z = -\partial_z p(\boldsymbol{r})\,\mathrm{d}V \quad (1.11)$$

which by the same means of the x- and y-component becomes

$$\mathrm{d}\boldsymbol{F} = -\nabla p(\boldsymbol{r})\mathrm{d}V \quad (1.12)$$

and once again by integrating the force becomes

$$\boldsymbol{F} = -\int_\Omega \nabla p(\boldsymbol{r})\,\mathrm{d}V \quad (1.13)$$

which tells us that integrating the pressure gradient in a volume Ω, is equivalent to integrating all of the infinitesimal contributions from pressure on the closed surface $\partial\Omega$,

$$\int_\Omega \nabla p(\boldsymbol{r})\,\mathrm{d}V = \oint_{\partial\Omega} p(\boldsymbol{r})\boldsymbol{n}\,\mathrm{d}A \quad (1.14)$$

which indeed is Gauss' theorem[1] in terms of pressure.

[1] see Eq. (B.8)

Chapter 2

Governing equations in fluid dynamics

2.1 The continuity equation

The governing equations are formulated by following the lecture notes [1, Bruus].

We consider an indeed arbitrary shaped region in space with volume Ω and surface $\partial\Omega$, see Fig. 2.1. The total mass of this region is given by integrating the density over the entire region

$$M(\Omega, t) = \int_\Omega \rho(\boldsymbol{r}, t)\, \mathrm{d}V, \tag{2.1}$$

where we can determine the rate of change in mass of the region Ω by taking the time derivative of the total mass $M(\Omega, t)$. Further, as indicated on Fig. 2.1, some current $\boldsymbol{J} = \rho(\boldsymbol{r}, t)\boldsymbol{v}(\boldsymbol{r}, t)$ (which is a mass current density in this case) flowing inside the region, can also potentially change the mass of the region, that is advection. The total mass is then also equal to the surface integral over $\partial\Omega$ of the mass current density, and we obtain

$$\partial_t M(\Omega, t) = \partial_t \int_\Omega \rho(\boldsymbol{r}, t)\, \mathrm{d}V = \oint_{\partial\Omega} (-\boldsymbol{n})\cdot\boldsymbol{J}(\boldsymbol{r}, t)\, \mathrm{d}A = \oint_{\partial\Omega} (-\boldsymbol{n})\cdot\rho(\boldsymbol{r}, t)\boldsymbol{v}\, \mathrm{d}A \tag{2.2}$$

Here $\boldsymbol{n}$ is the surface outward normal vector pointing outward from the surface at any particular point on a small part $\mathrm{d}A$ of the surface $\partial\Omega$, and hence $-\boldsymbol{n}$ implies that the mass current density is entering the region. Note that this principle apply

in general, regardless of what physical current $\boldsymbol{J}$ represents (e.g. charge, momenta, energy etc.). Since that the region is fixed in time, we can take the time derivative ∂_t inside the integral and apply Gauss' theorem, so

$$\partial_t M(\Omega,t) = \int_\Omega \mathrm{d}V\, \partial_t \rho(\boldsymbol{r},t) = \oint_{\partial\Omega} \mathrm{d}A\, (-\boldsymbol{n})\cdot\rho(\boldsymbol{r},t)\boldsymbol{v} = -\int_\Omega \mathrm{d}V\, \boldsymbol{\nabla}\cdot\rho(\boldsymbol{r},t)\boldsymbol{v} \quad (2.3)$$

and further utilize that the region Ω is arbitrary, from which it follows that the integrands must be identical. Obtaining directly from Eq. (2.3)

$$\partial_t \rho(\boldsymbol{r},t) = -\boldsymbol{\nabla}\cdot\rho(\boldsymbol{r},t)\boldsymbol{v}(\boldsymbol{r},t) \quad \text{or} \quad \partial_t\rho(\boldsymbol{r},t) = -\partial_j\rho(\boldsymbol{r},t)v_j \quad (2.4)$$

which is the continuity equation on vector and index notation[1], respectively. The continuity equation states that if density changes in time it is due to a divergence in the mass current density.

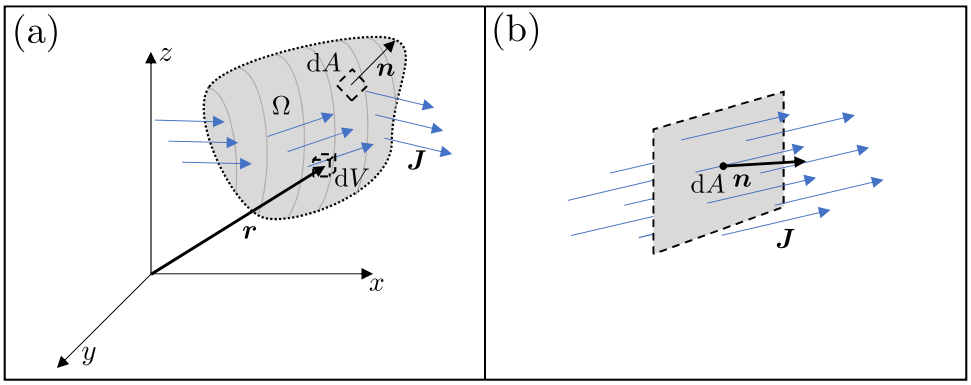

Figure 2.1: (a) Reference system showing the principle of an arbitrary current $\boldsymbol{J}$ inside a domain of fluid. The grey area Ω should be considered as a fixed and arbitrary region of continuous matter. (b) A generalized flux $\boldsymbol{J}\cdot\mathrm{d}\boldsymbol{A}$. with the normal defined as pointing outward with respect to the surface $\partial\Omega$ surrounding Ω.

2.2 The Navier-Stokes equation

In classical mechanics the dynamics of a system is governed by the acting forces which equals the rate of change in momentum, this is also the case in fluid dynamics. The momentum is defined as

$$\mathrm{d}P_i = v_i \mathrm{d}M = v_i \rho \mathrm{d}V, \quad (2.5)$$

[1]see appendix B.1 for details

identifying P_i as an extrinsic field the global momentum becomes

$$\partial_t P_i = \int_\Omega \partial_t v_i \rho \, \mathrm{d}V, \tag{2.6}$$

for a fixed volume Ω.

In general the forces can effectively be divided into two contributions, body and surface forces. In general there is a lot going on in the bulk e.g. interatomic interaction, but for now only long ranged forces are of interest, such as gravity. The body forces are written as $\boldsymbol{f}^b$, where the lowercase denotes that it is a force per unit volume. Considering the surface, all the information are in the stress tensor $\boldsymbol{\sigma}$, having the dimensions of forces per unit area. The sum of forces acting on the system becomes

$$\boldsymbol{F} = \int_\Omega \boldsymbol{f}^b \, \mathrm{d}V + \oint_{\partial\Omega} \boldsymbol{n} \cdot \boldsymbol{\sigma} \, \mathrm{d}A. \tag{2.7}$$

Since the rate of change in momentum (Newtons second law) equals the acting forces plus the advection of momentum, the dynamics becomes

$$\partial_t P_i = \int_\Omega \partial_t v_i \rho \, \mathrm{d}V = \int_\Omega f_i^b \, \mathrm{d}V + \oint_{\partial\Omega} \sigma_{ij} \, \mathrm{d}A_j - \oint_{\partial\Omega} n_j v_j \rho v_i \, \mathrm{d}A. \tag{2.8}$$

Solving this equation it is necessary to determine the stress tensor. As mentioned the stress tensor is force per unit area

$$\mathrm{d}\boldsymbol{F} = \boldsymbol{\sigma} \cdot \mathrm{d}\boldsymbol{A} \quad \text{or} \quad \mathrm{d}F_i = \sigma_{ij} \mathrm{d}A_j \tag{2.9}$$

noting the similarity between pressure and stress. Since the stress is defined as a tensor it describes the relation between forces and surfaces in space, see Fig. 1.2 (b). From Eq. (1.9) pressure is defined as the inward normal force on a surface hence the stress tensor will contain the mechanical pressure in the diagonal.

From Fig. 1.2 (b) a force acting on the surface can be divided into three categories; inward normal force - pressure, outward normal force - tension and a tangential force - shear. These information are also contained in the index notation, where the subscript i denotes the direction of which the force acts and the subscript j denotes the direction of the surface on which the force is acting on. If the stress components $\sigma_{ij} \neq \sigma_{ji}$ (consider Fig. 1.2) there will exist a torque and the elements will begin to rotate. In mechanical equilibrium this is not valid and the conclusion must be, that in mechanical equilibrium the stress tensor for a fluid must be symmetric by construction.

$$\boldsymbol{\sigma} = \boldsymbol{\sigma}^\intercal \quad \text{or} \quad \sigma_{ij} = \sigma_{ji} \tag{2.10}$$

The shear stress will naturally be induced by spatial variations in the velocity field. These variations can be fully described with the velocity gradient tensor $\partial_i v_j$. Assuming that there exists a linear relation of the form

$$\sigma_{ij} = -p\delta_{ij} + \eta\left(\partial_i v_j + \partial_j v_i\right) + (\beta - 1)\eta\partial_k v_k \delta_{ij}, \tag{2.11}$$

having the term $\partial_i v_j$ we must also have $\partial_j v_i$ ensuring that $\sigma_{ij} = \sigma_{ji}$. Fluids obeying this relation is said to be Newtonian.

Applying Gauss' theorem on Eq. (2.8) with a fixed volume Ω the equation become

$$\int_\Omega \partial_t(v_i\rho)\,\mathrm{d}V = \int_\Omega f_i^b\,\mathrm{d}V + \int_\Omega \partial_j\sigma_{ij}\,\mathrm{d}V - \int_\Omega \partial_j v_j \rho v_i\,\mathrm{d}V, \tag{2.12}$$

since this is true for any volume the integrands must be identical

$$\partial_t(v_i\rho) = f_i^b + \partial_j\sigma_{ij} - \partial_j v_j\rho v_i. \tag{2.13}$$

From the continuity equation Eq. (2.3) the rearranging of Eq. (2.13) becomes

$$\partial_t(v_i\rho) + \partial_j v_j\rho v_i = \rho\left(\partial_t + v_j\partial_j\right)v_i = f_i^b + \partial_j\sigma_{ij}. \tag{2.14}$$

Identifying the general Navier-Stokes equation

$$\rho\left(\partial_t + v_j\partial_j\right)v_i = \rho\frac{\mathrm{D}}{\mathrm{D}t}v_i = f_i^b + \partial_j\sigma_{ij} \tag{2.15a}$$

$$\rho\left(\partial_t + \boldsymbol{v}\cdot\boldsymbol{\nabla}\right)\boldsymbol{v} = \rho\frac{\mathrm{D}}{\mathrm{D}t}\boldsymbol{v} = \boldsymbol{f}^b + \boldsymbol{\nabla}\cdot\boldsymbol{\sigma}. \tag{2.15b}$$

The term on the left-hand side can be interpreted as the total acceleration by the material derivative in Eq. (1.7).

By taking the divergence of the stress tensor in Eq. (2.11) the Navier-Stokes eqaution becomes

$$\rho\left(\partial_t + v_j\partial_j\right)v_i = f_i^b - \partial_i p + \eta\left(\partial_j^2 v_i\right) + \beta\eta\partial_i\partial_j v_j \tag{2.16a}$$

$$\rho\left(\partial_t + \boldsymbol{v}\cdot\boldsymbol{\nabla}\right)\boldsymbol{v} = \boldsymbol{f}^b - \boldsymbol{\nabla}p + \eta\left(\nabla^2\boldsymbol{v}\right) + \beta\eta\boldsymbol{\nabla}\left(\boldsymbol{\nabla}\cdot\boldsymbol{v}\right) \tag{2.16b}$$

2.3 The equation of state

We will now consider the thermodynamics relating state variables with inspiration from the book[2, Blundell & Blundell]. Working with variables of state e.g. volume, pressure and density, it is adjacent to introduce the equation of state. Knowing the

temperature T and number of molecules N in a gas of volume V the equation of state f would take the form

$$p = f(T, N, V), \tag{2.17}$$

where

$$\mathrm{d}p = \left(\frac{\partial f}{\partial T}\right)_{\rho,V} \mathrm{d}T + \left(\frac{\partial f}{\partial N}\right)_{T,V} \mathrm{d}N + \left(\frac{\partial f}{\partial V}\right)_{T,N} \mathrm{d}V. \tag{2.18}$$

For an ideal gas one exact equation of state is

$$pV = Nk_BT = nRT \tag{2.19}$$

or

$$p = \frac{N}{V}k_BT = \frac{N_A}{\mathcal{M}}\rho k_BT = \rho R_sT. \tag{2.20}$$

Working with fluid systems actuated at frequencies around MHz the isentropic process[2] is a good approximation. For an isentropic process we know that the change in internal energy $\mathrm{d}U$ is due to the work $\mathrm{d}W$ done on the system

$$\mathrm{d}U = \mathrm{d}W, \tag{2.21}$$

which follows from the first law of thermodynamics, stating that the change in internal energy comes from the change in heat and the work. For an ideal gas the change in internal energy is given by $\mathrm{d}U = C_V\mathrm{d}T$ and the work as $\mathrm{d}W = -p\mathrm{d}V$, combining this with Eq. (2.19) the differentials becomes

$$C_V\mathrm{d}T = -p\mathrm{d}V = -\frac{N}{V}k_BT\mathrm{d}V. \tag{2.22}$$

Evaluating Eq. (2.22) the relation between volume and temperature for an adiabatic expansion becomes

$$\left(\frac{V_1}{V_2}\right)^{\frac{nR}{C_V}} = \left(\frac{T_2}{T_1}\right) \tag{2.23}$$

or formulated in another way

$$TV^{\gamma-1} = \text{constant}, \tag{2.24}$$

where $\frac{nR}{C_V} = \gamma - 1$ for an ideal gas, with the polytropic index γ. Since $pV \propto T$ and $\rho V = \text{constant}$ the relation between pressure and density becomes

$$\frac{p}{\rho^\gamma} = \text{constant}, \tag{2.25}$$

known as a polytropic form.

[2] no flow of heat and equivalent to an adiabatic expansion

Chapter 3

Perturbation theory in fluid dynamics

Working with frequencies in the MHz-domain a small actuation in the system can be regarded as small perturbations.

Identifying Eq. (2.16) as a nonlinear partial differential equation where the solutions are not general and there exists no unique solution, but with the theory of perturbation the problem can be decomposed into solvable equations.

3.1 First-order perturbation

The perturbation must be small (denoted with a subscript indicating the order)

$$|p_1| \ll p, \quad |\boldsymbol{v}_1| \ll \boldsymbol{v}, \quad \rho_1 \ll \rho. \tag{3.1}$$

By these means the field can be expanded to first order as

$$\rho = \rho_0 + \rho_1, \tag{3.2a}$$
$$p = p_0 + p_1, \tag{3.2b}$$
$$\boldsymbol{v} = \boldsymbol{v}_0 + \boldsymbol{v}_1. \tag{3.2c}$$

Assuming that the actuation happens so fast that the expansion can be assumed isentropic, the pressure field can be expanded in ρ as

$$p(\rho_) = p_0 + \left(\frac{\partial p(\rho_0)}{\partial \rho}\right)_s \rho_1 = p_0 + c_0^2 \rho_1, \tag{3.3}$$

assuming that there exists a linear relation between the pressure and density.

In the unperturbed system the velocity is set to zero, whereas the perturbed fields are

$$\rho(\boldsymbol{r},t) = \rho_0 + \rho_1(\boldsymbol{r},t), \tag{3.4}$$
$$p(\boldsymbol{r},t) = p_0 + c_0^2\rho_1(\boldsymbol{r},t), \tag{3.5}$$
$$\boldsymbol{v}(\boldsymbol{r},t) = \boldsymbol{0} + \boldsymbol{v}_1(\boldsymbol{r},t). \tag{3.6}$$

In the following the spatial and time dependence is omitted. With these relation the Navier-Stokes equation Eq. (2.16) can be evaluated to first order

$$\rho_0\partial_1\boldsymbol{v}_1 = -\boldsymbol{\nabla}p_1 + \eta\nabla^2\boldsymbol{v}_1 + \beta\eta\boldsymbol{\nabla}(\boldsymbol{\nabla}\cdot\boldsymbol{v}_1), \tag{3.7}$$

neglecting the body force.

To first order the continuity equation (2.3) is

$$\partial_t\rho_1 = -\rho_0\boldsymbol{\nabla}\cdot\boldsymbol{v}_1. \tag{3.8}$$

The equations can be related by taking the time derivative of Eq. (3.8)

$$\partial_t^2\rho_1 = -\rho_0\boldsymbol{\nabla}\cdot\partial_t\boldsymbol{v}_1 = \nabla^2 p_1 - (1+\beta)\eta\nabla^2(\boldsymbol{\nabla}\cdot\boldsymbol{v}_1), \tag{3.9}$$

using the relations $\boldsymbol{\nabla}\cdot\boldsymbol{v}_1 = -\frac{1}{\rho_0}\partial_t\rho_1$ and $p_1 = c_0^2\rho_1$ Eq. (3.9) becomes

$$\partial_t^2\rho_1 = \left[c_0^2 + \frac{(1+\beta)\eta}{\rho_0}\partial_t\right]\nabla^2\rho_1. \tag{3.10}$$

Within the scope of this project the actuation can be assumed harmonic in time i.e. every time dependent field gets the factor $\mathrm{e}^{-i\omega t}$. Since the fields of interest have the same time dependence the operator ∂_t can be replaced with $-i\omega$ and Eq. (3.10) becomes a linear partial differential equation

$$\nabla^2\rho_1 = -\frac{\omega^2}{c_0^2}\left[1 - i2\Gamma\right]^{-1}\rho_1, \tag{3.11}$$

where $\Gamma = \frac{(1+\beta)\eta\omega}{2\rho_0 c_0^2}$. For water at 25 °C the factor becomes $\Gamma \approx 8.2\times10^{-6}$ (given the values in table G.1.) i.e. rewriting the term to first order in Γ yields

$$k = \frac{\omega}{c_0}\left[1 - i2\Gamma\right]^{-1/2} \approx k_0\left[1 + i\Gamma\right], \tag{3.12}$$

yielding Helmholtz's equation for the acoustic density field

$$\nabla^2\rho_1 = -k^2\rho_1, \tag{3.13}$$

where the complex valued wavenumber means that the solutions will be damped waves, with a damping coefficient Γ. If $\Gamma \ll 1$ one must go to large distances before seeing any effect of the damping, since the characteristic length scale for the damping is $\frac{1}{k_0\Gamma}$. In the special case where $\eta = 0$ the solution will be waves propagating at group velocity c_0. Recall that $c_0^2 = \left(\frac{\partial p}{\partial \rho}\right)_s$ from Eq. (3.3), meaning that if the linear relation between pressure and density is known, for an adiabatic expansion, the speed of sound can be determined. From Eq. (2.25) the speed of sound for an ideal gas is

$$c_0 = \sqrt{\left(\frac{\partial p}{\partial \rho}\right)_s} = \sqrt{\gamma \frac{p}{\rho}}, \tag{3.14}$$

For the case where ρ_1 is proportional to p_1 then Eq. (3.13) is also valid for the pressure field, with the simple Cartesian solution

$$p_1(\boldsymbol{r}, t) = \left[p_+ \mathrm{e}^{i\boldsymbol{k}\cdot\boldsymbol{r}} + p_- \mathrm{e}^{-i\boldsymbol{k}\cdot\boldsymbol{r}}\right] \mathrm{e}^{-i\omega t}, \tag{3.15}$$

where $\boldsymbol{k} \cdot \boldsymbol{r} = k_x x + k_y y + k_z z$.

3.2 Second-order perturbation

In second-order perturbation we just add a third term in 3.2b and collect the second-order terms from Eq. (2.4) and Eq. (2.16) yielding

$$\partial_t \rho_2 = -\boldsymbol{\nabla} \cdot (\rho_0 \boldsymbol{v}_2 + \rho_1 \boldsymbol{v}_1), \tag{3.16}$$

$$\rho_0 \partial_t \boldsymbol{v}_2 + \rho_1 \partial_t \boldsymbol{v}_1 + \rho_0 (\boldsymbol{v}_1 \cdot \boldsymbol{\nabla}) \boldsymbol{v}_1 = -\boldsymbol{\nabla} p_2 + \eta \nabla^2 \boldsymbol{v}_2 + \beta \eta \boldsymbol{\nabla} (\boldsymbol{\nabla} \cdot \boldsymbol{v}_2). \tag{3.17}$$

Assuming harmonic time dependence the time average of these equations becomes

$$0 = -\rho_0 \boldsymbol{\nabla} \cdot \langle \boldsymbol{v}_2 \rangle - \boldsymbol{\nabla} \cdot \langle \rho_1 \boldsymbol{v}_1 \rangle \tag{3.18}$$

$$\langle \rho_1 \partial_t \boldsymbol{v}_1 \rangle + \rho_0 \langle (\boldsymbol{v}_1 \cdot \boldsymbol{\nabla}) \boldsymbol{v}_1 \rangle = -\boldsymbol{\nabla} \langle p_2 \rangle + \eta \nabla^2 \langle \boldsymbol{v}_2 \rangle + \beta \eta \boldsymbol{\nabla} (\boldsymbol{\nabla} \cdot \langle \boldsymbol{v}_2 \rangle), \tag{3.19}$$

since the product of two first-order terms does not equal zero, when taking the time average i.e. product of terms proportional to harmonics such as cosines and sines, equals $\langle \sin^2(\omega t) \rangle = \langle \cos^2(\omega t) \rangle = \frac{1}{2}$.

For inviscid bulk ($\eta = 0$) the velocity can be described with a velocity potential i.e. $\boldsymbol{\nabla} \times \boldsymbol{v}_1 = 0$ and $(\boldsymbol{v}_1 \cdot \boldsymbol{\nabla}) \boldsymbol{v}_1 = \frac{1}{2} \boldsymbol{\nabla} v_1^2$, from this Eq. (3.19) becomes

$$\begin{aligned} -\boldsymbol{\nabla} \langle p_2 \rangle &= -\frac{1}{c_0^2 \rho_0} \langle p_1 \boldsymbol{\nabla} p_1 \rangle + \frac{1}{2} \rho_0 \langle \boldsymbol{\nabla} v_1^2 \rangle \\ &= -\frac{1}{2 c_0^2 \rho_0} \boldsymbol{\nabla} \langle p_1^2 \rangle + \frac{1}{2} \rho_0 \boldsymbol{\nabla} \langle v_1^2 \rangle \end{aligned} \tag{3.20}$$

and the time-averaged second-order pressure field takes the form

$$\langle p_2 \rangle = \frac{1}{2}\kappa_0 \left\langle p_1^2 \right\rangle - \frac{1}{2}\rho_0 \left\langle v_1^2 \right\rangle, \tag{3.21}$$

where we have defined the compressibility $\kappa_0 = \frac{1}{\rho_0 c_0^2}$.

Chapter 4

Acoustic resonances

4.1 Harmonic fields and acoustic energy

Working with small harmonic actuating in the sense that Eq. (3.1) is valid, then from the theory of first-order perturbation the acoustics of a fluid system are developed. In most cases analytical solutions requires high symmetry and well-known boundary conditions.

To get a feeling of the acoustics we consider a potential flow i.e. $\boldsymbol{\nabla} \times \boldsymbol{v}_1 = \boldsymbol{0}$ implying $\boldsymbol{\nabla}(\boldsymbol{\nabla} \cdot \boldsymbol{v}_1) = \nabla^2 \boldsymbol{v}_1$ and that the velocity field can be written as a gradient of a potential $\boldsymbol{v}_1 = \boldsymbol{\nabla}\varphi_1$. Under these conditions Eq. (3.7) can be rewritten as

$$\rho_0 \partial_t \boldsymbol{v}_1 = -\boldsymbol{\nabla} p_1 + (1+\beta)\eta \boldsymbol{\nabla}(\boldsymbol{\nabla} \cdot \boldsymbol{v}_1), \tag{4.1}$$

imposing the harmonic time dependence and $\boldsymbol{\nabla} \cdot \boldsymbol{v}_1 = i\frac{\omega}{c_0^2 \rho_0} p_1$ from first-order continuity, the velocity can be written as

$$\boldsymbol{v}_1 = \boldsymbol{\nabla}\varphi_1 = -\frac{i}{\omega\rho_0}\left(1 - 2i\Gamma\right)\boldsymbol{\nabla} p_1 \approx -\frac{i}{\omega\rho_0(1+i\Gamma)^2}\boldsymbol{\nabla} p_1. \tag{4.2}$$

This shows that the velocity potential is proportional to the pressure field, therefore the solution for the velocity potential must be of the form

$$\varphi_1(\boldsymbol{r}, t) = \left[\varphi_+ \mathrm{e}^{i\boldsymbol{k}\cdot\boldsymbol{r}} + \varphi_- \mathrm{e}^{-i\boldsymbol{k}\cdot\boldsymbol{r}}\right] \mathrm{e}^{-i\omega t} \tag{4.3}$$

as in Eq. (3.15). This means that for a potential flow the acoustic velocity field will have the form

$$\boldsymbol{v}_1(\boldsymbol{r}, t) = \boldsymbol{\nabla}\varphi_1 = i\boldsymbol{k}\left[\varphi_+ \mathrm{e}^{i\boldsymbol{k}\cdot\boldsymbol{r}} - \varphi_- \mathrm{e}^{-i\boldsymbol{k}\cdot\boldsymbol{r}}\right] \mathrm{e}^{-i\omega t} \tag{4.4}$$

Lets consider the case of a planar flow where $\boldsymbol{v}_1(\boldsymbol{r},t) = v_1(x,t)\hat{\boldsymbol{e}}_x$ yielding

$$v_1(x,t) = ik\left[\varphi_+ \mathrm{e}^{ikx} - \varphi_- \mathrm{e}^{-ikx}\right]\mathrm{e}^{-i\omega t}. \tag{4.5}$$

To determine a unique expression for the velocity, boundary conditions are needed. For simplicity we will consider the antisymmetric boundary condition at $\pm L$ with an amplitude $\omega\ell$, which leads to

$$v_1(L,t) = -v_1(-L,t) = \omega\ell \mathrm{e}^{-i\omega t} \tag{4.6}$$

or

$$\varphi_+ = \varphi_- = -\frac{\omega\ell}{2k\sin(kL)} \tag{4.7}$$

with the unique solution

$$v_1(x,t) = \omega\ell\frac{\sin(kx)}{\sin(kL)}\mathrm{e}^{-i\omega t} = \frac{\sin(k_0[1+i\Gamma]x)}{\sin(k_0[1+i\Gamma]L)}\mathrm{e}^{-i\omega t}. \tag{4.8}$$

Acoustic resonances can be identified when the velocity is at its maximum i.e. when $\sin(kL)$ is minimum. Finding the minimum, one can do an approximation as in Eq. (3.12), but where $\Gamma k_0 L \ll 1$ yielding

$$v_1(x,t) \approx \omega\ell\frac{\sin(k_0x) + i\Gamma k_0 x\cos(k_0x)}{\sin(k_0L) + i\Gamma k_0 L\cos(k_0L)}\mathrm{e}^{-i\omega t}. \tag{4.9}$$

Since the Γ-term is much smaller than unity, the resonance condition becomes

$$k_0 L = n\pi, \quad \text{for all} \quad n \in \mathbb{N}. \tag{4.10}$$

Defining the resonance wavenumber $k_n = \frac{n\pi}{L}$. At resonance the velocity field will be

$$v_1(x,t) \approx (-1)^n\omega_n\ell\left[\frac{x}{L}\cos\Big(n\pi\frac{x}{L}\Big) - \frac{i}{\Gamma n\pi}\sin\Big(n\pi\frac{x}{L}\Big)\right]\mathrm{e}^{-i\omega_n t}, \tag{4.11}$$

where the resonance frequency is defined as $\omega_n = k_n c_0$ accomplished by tuning the actuation frequency.

For a harmonically oscillating system the energy is two times the averaged kinetic energy - a general result for harmonic mechanics. In relation to fluid dynamics it is natural to work with the energy density E_{ac}. For the harmonically oscillating system we find that

$$\begin{aligned} E_{ac} = 2\left\langle E_{kin}\right\rangle &= 2\frac{1}{2L}\int_{-L}^{L}\frac{1}{2}\rho_0\left|\langle v_1(x,t)\rangle\right|^2\mathrm{d}x \\ &= \frac{1}{2L}\int_{-L}^{L}\frac{1}{2}\rho_0\left|\omega\ell\frac{\sin(kx)}{\sin(kL)}\right|^2\mathrm{d}x = \frac{1}{4}\rho_0\omega^2\ell^2\frac{1}{\left|\sin(kL)\right|^2}. \end{aligned} \tag{4.12}$$

In practice the frequency can be controlled, which makes it relevant to expand $\sin(kL)$ around the resonances k_nL

$$E_{ac} = \frac{1}{4}\rho_0\omega^2\ell^2\frac{1}{|\sin(kL)|^2} \approx \frac{1}{4}\rho_0\omega^2\ell^2\frac{1}{|(kL-k_nL)|^2} = \frac{1}{4}\frac{\rho_0\omega^2\ell^2}{n^2\pi^2}\frac{\omega_n^2}{(\omega-\omega_n)^2+\Gamma^2\omega_n^2}, \tag{4.13}$$

which is a single peaked function centered around the resonance frequency ω_n. The expression has the shape as a Lorentzian function and has full width at half maximum $\Delta\omega = 2\Gamma\omega_n$, see Fig. D.1, making it relevant to define the quality factor

$$Q = \frac{\omega_n}{\Delta\omega} = \frac{1}{2\Gamma}. \tag{4.14}$$

With a damping factor $\Gamma = 0.004$ as in [3], the quality factor yields $Q = 125$, whereas the theory yields $Q \approx 1 \times 10^5$.

The energy in Eq. (4.13) is a special case of a harmonic standing pressure wave i.e. acoustic resonance, but in general the acoustic energy density will be

$$E_{ac} = \langle E_{kin}\rangle + \langle E_{pot}\rangle\,. \tag{4.15}$$

The kinetic energy density are $E_{kin} = \frac{1}{2}\rho|v(\boldsymbol{r},t)|^2$ where the potential energy density in acoustics are

$$E_{pot} = -\frac{1}{V}\int p\,\mathrm{d}V. \tag{4.16}$$

As in Eq. (2.25) the relation $\rho V =$ constant were used, which means that $\rho\mathrm{d}V + V\mathrm{d}\rho = 0$ or $\mathrm{d}V = -\frac{V}{\rho}\mathrm{d}\rho$. Since the linear relation between ρ and p are known to be $\frac{\mathrm{d}p}{\mathrm{d}\rho} = c_0^2$ from Eq. (3.3), the potential energy density can be evaluated as

$$E_{pot} = -\frac{1}{V}\int p\mathrm{d}V = \frac{1}{V}\int p\frac{V}{\rho}\frac{\mathrm{d}p}{c_0^2} = \frac{1}{2}\frac{p^2}{\rho c_0^2}. \tag{4.17}$$

Working with harmonics the average will contribute with a factor $\frac{1}{2}$, evidently the acoustic energy density will have the form

$$E_{ac} = \langle E_{kin}\rangle + \langle E_{pot}\rangle = \frac{1}{4}\rho|v|^2 + \frac{1}{4}\kappa_0|p|^2. \tag{4.18}$$

4.2 Acoustic forces

A particle with radius a placed in a quiescent fluid will experience both buoyant and gravity as in Eq. (2.7), but if the fluid is not at rest i.e. actuated at MHz frequencies,

there will be a second order effect. If the particle is compressible and the radius a is much smaller than the acoustic wavelength, it will induce a scattered wave i.e. the first order velocity will consist of an incoming and scattering term

$$\boldsymbol{v}_1 = \boldsymbol{v}_{in} + \boldsymbol{v}_{sc}. \tag{4.19}$$

Calculating the effect of the scattered wave, one must determine $\boldsymbol{v}_{sc}$. In an inviscid bulk the velocity field can be described with a potential as in Eq. (4.2)

$$\boldsymbol{v}_1 = \boldsymbol{\nabla}\varphi_1 = \boldsymbol{\nabla}\varphi_{in} + \boldsymbol{\nabla}\varphi_{sc}, \tag{4.20}$$

where both terms obeys Helmholtz's equation Eq. (3.13) since $\varphi \propto p$. The first order pressure field Eq. (4.2) becomes

$$p_1 = i\omega\rho_0 \left(\varphi_{in} + \varphi_{sc}\right), \tag{4.21}$$

where the damping factor is set to zero.

The scattered wave give rise to a radiation force $\boldsymbol{F}^{rad}$, which is a second-order time-averaged effect and Eq. (2.8) can be written as

$$\begin{aligned} \boldsymbol{F}^{rad} &= -\oint_{\partial\Omega} \left(\langle p_2 \rangle \boldsymbol{n} + \rho_0 \langle (\boldsymbol{v}_1 \cdot \boldsymbol{n})\boldsymbol{v}_1 \rangle\right) \mathrm{d}A \\ &= -\oint_{\partial\Omega} \left[\left(\frac{1}{2}\kappa_0 \langle p_1^2 \rangle - \frac{1}{2}\rho_0 \langle v_1^2 \rangle\right)\boldsymbol{n} + \rho_0 \langle (\boldsymbol{v}_1 \cdot \boldsymbol{n})\boldsymbol{v}_1 \rangle\right] \mathrm{d}A, \end{aligned} \tag{4.22}$$

for $\eta = 0$. To ease the evaluation of this integral, it is reasonable to only consider the mixed product between the incoming and scattered wave. Since the square of each field consists of three contributions: φ_{in}^2 containing no information about the interference, φ_{sc}^2 which scales with the square of the particle volume and $\varphi_{in}\varphi_{sc}$ which is the dominant term. Rewriting the integral yields

$$\begin{aligned} \boldsymbol{F}^{rad} &= -\int_\Omega \rho_0 \left\langle \boldsymbol{v}_{in} \left(\nabla^2 - \frac{1}{c_0^2}\partial_t^2\right)\varphi_{sc} \right\rangle \mathrm{d}V \\ &= -\frac{4}{3}\pi a^3 \left(\frac{1}{2}\kappa_0 \,\mathrm{Re}\{f_1^* p_{in}^* \boldsymbol{\nabla} p_{in}\} - \frac{3}{4}\rho_0 \,\mathrm{Re}\{f_2^* \boldsymbol{v}_{in}^* \cdot \boldsymbol{\nabla}\boldsymbol{v}_{in}\}\right), \end{aligned} \tag{4.23}$$

where f_1 and f_2 are scattering coefficients (see [4] for details). In the absence of viscosity these coefficients are real and given by

$$f_1 = 1 - \tilde{\kappa}, \tag{4.24a}$$

$$f_2 = \frac{2(\tilde{\rho} - 1)}{2\tilde{\rho} + 1}, \tag{4.24b}$$

where $\tilde{\kappa} = \kappa_p/\kappa_0$ and $\tilde{\rho} = \rho_p/\rho_0$ is the relative compressibility and density respectively. The subscript p denotes the particle and the subscript zero is water. These expressions for the scattering coefficients are used unless otherwise stated.

The classic result for the radiation force can be presented for 1D standing waves, which is the case treated in this thesis, for cosine dependant waves with wave-number $k = \frac{2\pi}{\lambda}$ as

$$F_{1D}^{rad} = 4\pi\Phi a^3 k E_{ac} \sin(2k_y y) \tag{4.25a}$$

$$\Phi = \frac{1}{3}f_1 + \frac{1}{2}f_2 \tag{4.25b}$$

where Φ is the so called acoustophoretic contrast factor, which in the complete model also depends on the boundary layer thickness. However for inviscid bulk it can be calculated using the coefficients in Eq. (4.24).

When submerging a particle of radius a and density ρ_p, it will experience a buoyant force F_b. Naturally the gravitational force F_g is also exerting a force on the particle opposite to the buoyant force. It is useful when comparing the magnitudes of acting forces, to look at the buoyancy compensated gravitational force exerted on such a particle, which is given by

$$F_g^{comp} = \frac{4}{3}\pi\rho_f(\tilde{\rho} - 1)a^3 g. \tag{4.26}$$

Here ρ_f is the density of the fluid in which the particle is submerged and g is the gravitational acceleration. If the viscous forces are dominant, that is if the Reynolds number $\mathrm{Re} = \frac{\eta v a}{\rho_F} = \frac{va}{\nu_k} \ll 1$, (The kinematic viscosity ν_k, is not to be confused with Poisson's ratio ν, which will be presented in Chapter 5) then the frictional forces will yield

$$F_d = 6\pi\eta a v. \tag{4.27}$$

known as Stokes' drag force.

Chapter 5

Linear theory of elastic solids

The foundation of acoustic wave theory in elastic solids is formulated in the following, on basis of the book by [5, Lautrup] and notes by [6, Bruus]. This will form the foundation for our further studies in microscale acoustofluidics and the coupling between elastic solids and Newtonian fluids.

5.1 The displacement field and strain

The displacement field is a quantity describing the macroscopic deformation of a body, by means of its constituents (material particles) generally displaced simultaneously. Consider the original position $\boldsymbol{R}$ as a function of actual position $\boldsymbol{r}$ denoted by $\boldsymbol{R}(\boldsymbol{r})$, then the displacement field is given by

$$\boldsymbol{u}(\boldsymbol{r}) = \boldsymbol{r} - \boldsymbol{R}(\boldsymbol{r}). \tag{5.1}$$

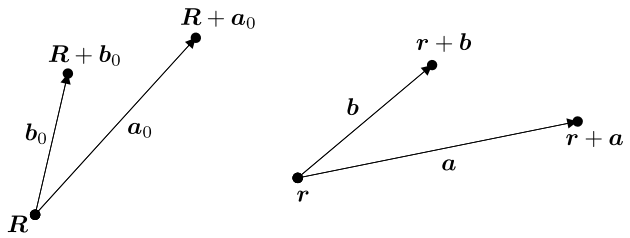

Figure 5.1: Depiction of infinitesimal material needle displaced from $\boldsymbol{a_0}$ to $\boldsymbol{a}$ and $\boldsymbol{b_0}$ to $\boldsymbol{b}$, illustrating the concept of displacement.

As seen in Fig. 5.1 a material particle "needle" is connecting points $\boldsymbol{R}$ and $\boldsymbol{R}+\boldsymbol{a_0}$ in space in a Cartesian coordinate system in terms of the vector $\boldsymbol{a_0}$. This is describing

the system before displacement. Right after displacement, the point is now followed to the positions $\boldsymbol{r}$ and $\boldsymbol{r}+\boldsymbol{a}$ interconnected by the vector $\boldsymbol{a}$. By the definition of Eq. (5.1) and expanding to first order in $\boldsymbol{a}$ it is obtained that the displacement is

$$\begin{aligned}\boldsymbol{u}(\boldsymbol{r}+\boldsymbol{a})-\boldsymbol{u}(\boldsymbol{r}) &= [(\boldsymbol{r}+\boldsymbol{a})-\boldsymbol{R}(\boldsymbol{r}+\boldsymbol{a})]-[\boldsymbol{r}-\boldsymbol{R}(\boldsymbol{r})] \\ &= \boldsymbol{a}-\boldsymbol{a_0} \\ &= (\boldsymbol{a}\cdot\boldsymbol{\nabla})\boldsymbol{u}(\boldsymbol{r})+\mathcal{O}(\boldsymbol{a}^2)\end{aligned} \tag{5.2}$$

which makes us able to conclude that displacement of a "material needle" of infinitesimal proportions changes as

$$\delta\boldsymbol{a} \equiv \boldsymbol{a}-\boldsymbol{a_0} = (\boldsymbol{a}\cdot\boldsymbol{\nabla})\boldsymbol{u}(\boldsymbol{r}). \tag{5.3}$$

Consider again the situation depicted in Fig. 5.1, where the displacement of the pairs of material needles is treated. The scalar product of the displacement needles $\boldsymbol{a}\cdot\boldsymbol{b}$ is invariant under translation and rotation, thus also an indicator for geometrical changes. By use of Eq. (5.3) the change of the scalar product $\delta(\boldsymbol{a}\cdot\boldsymbol{b}) = \delta\boldsymbol{a}\cdot\boldsymbol{b}+\boldsymbol{a}\cdot\delta\boldsymbol{b}$ becomes

$$\begin{aligned}\boldsymbol{a}\cdot\boldsymbol{b}-\boldsymbol{a_0}\cdot\boldsymbol{b_0} &= \boldsymbol{a}\cdot\boldsymbol{b}-[\boldsymbol{a}-(\boldsymbol{a}\cdot\boldsymbol{\nabla})\boldsymbol{u}]\cdot[\boldsymbol{b}-(\boldsymbol{b}\cdot\boldsymbol{\nabla})\boldsymbol{u}] \\ &= 2\boldsymbol{a}\cdot\boldsymbol{s}\cdot\boldsymbol{b}+\mathcal{O}(\boldsymbol{u}^2)\end{aligned} \tag{5.4}$$

Evidently, Cauchy's strain tensor (which is symmetric by construction)

$$s_{ij} = \frac{1}{2}(\partial_i u_j+\partial_j u_i) \quad \text{or} \quad \boldsymbol{s} = \frac{1}{2}(\boldsymbol{\nabla}\boldsymbol{u}+(\boldsymbol{\nabla}\boldsymbol{u})^{\intercal}). \tag{5.5}$$

appears in the scalar product between the pair of material needles, and indeed is the measure of local deformation. Note that Cauchy's strain tensor is only valid for $|\boldsymbol{\nabla}\boldsymbol{u}| \ll 1$, thus the induced error is proportional to the magnitude of the displacement gradient. However, the limit holds for magnitudes of displacement gradients concerning investigations that will be carried out in this thesis.

5.2 Mechanical equilibrium

The sum of forces acting in continuum theory is the superposition of acting surface forces and body forces. With the force originating from surface forces or stress Eq.

2.9 and the body forces as $\mathrm{d}\boldsymbol{F} = \boldsymbol{f}^{in}\mathrm{d}V$, then the total force, will be given as

$$\boldsymbol{F} = \int_\Omega \boldsymbol{f}_{in}\,\mathrm{d}V \equiv \int_\Omega \boldsymbol{f}\,\mathrm{d}V + \oint_{\partial\Omega} \boldsymbol{\sigma}\cdot\mathrm{d}\boldsymbol{A}. \tag{5.6}$$

In mechanical equilibrium the force must be zero, since otherwise will result in movement of the body. Thus the state of mechanical equilibrium $\boldsymbol{f}^{in} = \boldsymbol{0}$ results in

$$\boldsymbol{f} + \boldsymbol{\nabla}\cdot\boldsymbol{\sigma} = \boldsymbol{0} \quad \text{or} \quad f_i + \partial_j\sigma_{ij} = 0 \tag{5.7}$$

by using Gauss' theorem on the surface integral of Eq. (5.6) to obtain Cauchy's equilibrium equation.

5.3 The stress tensor

Once again we consider a region Ω with closure $\partial\Omega$ consisting of an elastic solid with zero net charge locally. Having an intrinsic force field $\boldsymbol{f}^{in}$ driven by a displacement field $\boldsymbol{u}$, the force is required to be of short-ranged nature in a continuum. Consequently, the forces will mutually cancel out in the interior of the volume Ω, leaving only the force contribution from the surface (stress), thus one must demand

$$\int_\Omega \boldsymbol{f}^{in}\,\mathrm{d}V = \oint_{\partial\Omega} \boldsymbol{\sigma}\cdot\boldsymbol{n}\,\mathrm{d}A = \int_\Omega \boldsymbol{\nabla}\cdot\boldsymbol{\sigma}\,\mathrm{d}V \tag{5.8}$$

hence it can be concluded that the intrinsic force must be $\boldsymbol{f}^{in} = \boldsymbol{\nabla}\cdot\boldsymbol{\sigma}$. By the same principles stated in the discussions of section 2.2 and shown in eqs. 2.7 to 2.10, the stress tensor for elastic solids must also be symmetric. Now the volume Ω with surface $\partial\Omega$ interfacing vacuum (i.e. $\boldsymbol{\sigma}\cdot\boldsymbol{n} = \boldsymbol{0}$) is experiencing intrinsic force density $\boldsymbol{f}^{in}$ driven by infinitesimal interior displacement fields $\delta\boldsymbol{u}$. Henceforth, the system will experience a mechanical work from the displacement-driven force as

$$\begin{aligned}\int_\Omega \delta W \,\mathrm{d}V &= \int_\Omega f_i^{in}\,\delta u_i \,\mathrm{d}V = \int_\Omega \delta u_i \partial_j \sigma_{ij} \,\mathrm{d}V \\ &= \oint_{\partial\Omega} \delta u_i \sigma_{ij} n_j \,\mathrm{d}A - \int_\Omega \partial_j(\delta u_i)\sigma_{ij} \,\mathrm{d}V \\ &= -\frac{1}{2}\int_\Omega \partial_j(\delta u_i)\sigma_{ij} \,\mathrm{d}V - \frac{1}{2}\int_\Omega \partial_j(\delta u_i)\sigma_{ij} \,\mathrm{d}V \\ &= -\frac{1}{2}\int_\Omega \sigma_{ij}[\partial_i(\delta u_j) + \partial_j(\delta u_i)]\mathrm{d}V \\ &= -\int_\Omega \sigma_{ij}\,\delta s_{ij} \,\mathrm{d}V\end{aligned} \tag{5.9}$$

and evidently by looking at the integrands, it is obtained that mechanical work in such a system is relating the stress and strain by

$$\delta W = -\sigma_{ij}\,\delta s_{ij}. \tag{5.10}$$

Using that the infinitesimal change in free energy F, by the thermodynamic relation, is due to

$$\mathrm{d}F = -S\mathrm{d}T - \mathrm{d}W = -S\mathrm{d}T + \sigma_{ij}\mathrm{d}s_{ij} \tag{5.11}$$

and ensuring isothermal conditions such that the entropy S vanishes, it can be obtained that the stress of elastic solids is given as the strain derivative of the free energy

$$\sigma_{ij} = \left(\frac{\partial F}{\partial s_{ij}}\right)_T. \tag{5.12}$$

Thus for the case of a system in thermal equilibrium, both the stress tensor $\boldsymbol{\sigma}$ and the strain tensor $\boldsymbol{s}$ ought to be zero. This implies that the obtained result for the stress Eq. (5.12) implies a free energy F in the quadratic form

$$F = F_0 + \frac{1}{2}C_{ijkl}s_{ij}s_{kl} \tag{5.13}$$

denoting an elastic modulus tensor of rank four C_{ijkl}, and the stress tensors for a total of 81 combined geometrically dependant directions. Since that the treated elastic solids of this report are assumed to be of isotropic nature, the quadratic equation Eq. (5.13) reduces to

$$F = F_0 + \frac{1}{2}\lambda(s_{kk})^2 + \mu s_{ij}s_{ij} \tag{5.14}$$

where it is utilized that the only two directions surviving when considering isotropic solids are $[\mathrm{Tr}(\boldsymbol{s})]^2 = (s_{kk})^2 = (\boldsymbol{\nabla} \cdot \boldsymbol{u})^2$ and $\mathrm{Tr}(\boldsymbol{s} \cdot \boldsymbol{s}) = s_{ij}s_{ij}$ with the so called Lamé coefficients μ (shear modulus or modulus of rigidity) and λ (no special name), which are parameters describing the material properties. By the definition of the stress-strain relation Eq. (5.12) the stress tensor becomes

$$\sigma_{ij} = \lambda s_{kk}\delta_{ij} + 2\mu s_{ij}. \tag{5.15}$$

The strain tensor itself is a dimensionless quantity, yielding the Lamé units coefficients $[\mu] = [\lambda] = \mathrm{Pa}$ justifying the relation to the stress tensor $[\sigma_{ij}] = \mathrm{Pa}$.

5.4 Elastic parameters

Imagine a long straight rod situated along the x-axis of a traditional Cartesian coordinate system. Hooke's law states that the force required to prolong a rod of length L by an amount x is $F = kx$, where k is the spring constant. Considering linearly elastic and isotropic solids the force must be proportional to the cross-sectional area A of the rod. Taking an ensemble of N rods with this area yields that the total force required to extend the rod is Nkx for uniform changes of length of the ensemble of rods. Hence the quantity of interest is rather the normal stress $\sigma_{xx} = \frac{NF}{NA} = \frac{Nkx}{NA} = \frac{kx}{A}$, which indeed is independent by number of rods N and area A. Since the force F must act on each cross-section, it follows that the stress must be the same in every point along the rod. Furthermore, this uniform distribution of stress suggests that the ratio between the extension x and length L of the rod must equal the ratio of a shorter part of the rod $L' < L$ extended by $x' < x$ as $\frac{x'}{L'} = \frac{x}{L}$. Consequently, it appears that relative elongation i.e. the strain $s_{xx} = \frac{x}{L}$, is more fundamental when describing the rod, in contrary to the absolute length change x. Thus, Young's modulus is neatly introduced as

$$E = \frac{\sigma_{xx}}{s_{xx}} = \frac{F/A}{x/L} \tag{5.16}$$

In the vast majority of linear elastic solids the elongation of such a rod, will induce a change of the dimensions both in longitudinal and transverse directions. Elongation in the longitudinal direction yields a contraction of the transverse direction, which can be described as a strain $s_{yy} = h/D$. Where h is the magnitude of contraction due to the force elongating the rod. Positive stretching of linearly elastic solids is proportional to the stretching force F, thus $\frac{s_{yy}}{s_{xx}}$ is independent of F and the negative

of this ratio

$$\nu = -\frac{s_{yy}}{s_{xx}} \tag{5.17}$$

indeed is Poisson's ratio. By the definition of stress Eq. (5.15), and the rod along the x-axis, it can be obtained that

$$\sigma_{xx} = \lambda s_{kk} + 2\mu s_{xx} \tag{5.18a}$$
$$0 = \lambda s_{kk} + 2\mu s_{yy} \tag{5.18b}$$
$$0 = \lambda s_{kk} + 2\mu s_{zz} \tag{5.18c}$$

Rearranging and adding Eq. 5.18b and Eq. 5.18c gives $(2\lambda + 2\mu)s_{kk} - 2\mu s_{xx} = 0$ which then is rewritten as $\frac{s_{kk}}{s_{xx}} = \frac{\mu}{\lambda+\mu}$. With Eq. 5.18b it is seen that $\lambda s_{kk} = -2\mu s_{yy}$, by dividing both sides by s_{xx} and rewriting, one gets $\nu = -\frac{s_{yy}}{s_{xx}} = \frac{\lambda}{2\mu}\frac{s_{kk}}{s_{xx}} = \frac{\lambda}{2(\mu+\lambda)}$. Finally Eq. 5.18a multiplied by $\frac{1}{s_{xx}}$ gives $E = \frac{\sigma_{xx}}{s_{xx}} = \lambda\frac{s_{kk}}{s_{xx}} + 2\mu = \frac{\mu\lambda}{\mu+\lambda} + 2\mu$, which then can be solved for μ and λ to give

$$\mu = \frac{1}{2(\nu+1)}\,E \tag{5.19a}$$
$$\lambda = \frac{\nu}{(1-2\nu)(1+\nu)}\,E. \tag{5.19b}$$

5.5 The equation of motion

If Eq. (5.7), Eq. (5.15) and Eq. (5.5) is combined by insertion of the latter two equations in the first, it is obtained that

$$f_i + \lambda\partial_j\partial_k u_k + \mu\partial_j(\partial_i u_j + \partial_j u_i) = 0 \tag{5.20a}$$
$$\boldsymbol{f} + \mu\nabla^2\boldsymbol{u} + (\mu+\lambda)\boldsymbol{\nabla}(\boldsymbol{\nabla}\cdot\boldsymbol{u}) = \boldsymbol{0} \tag{5.20b}$$

which is the expression also know as Navier-Cauchy equilibrium equation. The proper position of a displaced particle is a function of time, but only with regards to the displacement $\boldsymbol{u}(\boldsymbol{r},t)$. Hence the velocity of that material particle, must be $\boldsymbol{v}(\boldsymbol{r},t) = \partial_t\boldsymbol{u}(\boldsymbol{r},t)$ with acceleration $\boldsymbol{a}(\boldsymbol{r},t) = \partial_t^2\boldsymbol{u}(\boldsymbol{r},t)$. The total force is acting on each and every material particle in a given volume. Newtons second law for

material particles is stated as $\mathrm{d}M\boldsymbol{a} = \boldsymbol{f}^{in}\mathrm{d}V$, so dividing with the volume and use Eq. (5.20a) makes one arrive at

$$\rho\partial_t^2\boldsymbol{u} = \boldsymbol{f} + \mu\nabla^2\boldsymbol{u} + (\mu+\lambda)\boldsymbol{\nabla}(\boldsymbol{\nabla}\cdot\boldsymbol{u}) \tag{5.21}$$

the Navier's equation of motion.

5.6 Longitudinal and transverse displacement fields

The equation of motion can be used to obtain the wave equation. The only difference between the wave equation for small amplitude acoustic waves in fluids to that of elastic solids is the dimensions. The field in a fluid is represented as either a pressure- or density field, which is a scalar field. In elastic solids the vector field $\boldsymbol{u}$ can be represented by acoustic waves. Theoretically the waves of this displacement vector field, can be entirely split up in two independent directions, respectively, in longitudinal and transverse components. A Helmholtz decomposition of the displacement field $\boldsymbol{u}$ ensures a divergence-free transverse component and irrotational longitudinal component, as

$$\boldsymbol{u} = \boldsymbol{u}_L + \boldsymbol{u}_T \tag{5.22a}$$
$$0 = \boldsymbol{\nabla}\cdot\boldsymbol{u}_T \tag{5.22b}$$
$$\boldsymbol{0} = \boldsymbol{\nabla}\times\boldsymbol{u}_L. \tag{5.22c}$$

Using a vector identity as $\boldsymbol{\nabla}(\boldsymbol{\nabla}\cdot\boldsymbol{u}) = \nabla^2\boldsymbol{u} + \boldsymbol{\nabla}\times(\boldsymbol{\nabla}\times\boldsymbol{u})$ together with above Eqs. Eq. (5.22) the relations

$$\nabla^2\boldsymbol{u} = \nabla^2\boldsymbol{u}_L + \nabla^2\boldsymbol{u}_T \tag{5.23a}$$
$$\boldsymbol{\nabla}(\boldsymbol{\nabla}\cdot\boldsymbol{u}) = \boldsymbol{\nabla}(\boldsymbol{\nabla}\cdot\boldsymbol{u}_L) = \nabla^2\boldsymbol{u}_L \tag{5.23b}$$

are obtained. Inserting these relations into Navier's equation of motion Eq. (5.21) the wave equation reveals itself for the directions as

$$\begin{aligned}\rho(\partial_t^2\boldsymbol{u}_L + \partial_t^2\boldsymbol{u}_T) &= \mu\nabla^2\boldsymbol{u}_L + \mu\nabla^2\boldsymbol{u}_T + (\mu+\lambda)\nabla^2\boldsymbol{u}_L. \\ &= (2\mu+\lambda)\nabla^2\boldsymbol{u}_L + \mu\nabla^2\boldsymbol{u}_T\end{aligned} \tag{5.24}$$

Broken up in longitudinal and transverse waves, the resulting equations are

$$\partial_t^2 \boldsymbol{u}_L = \frac{(2\mu+\lambda)}{\rho}\nabla^2 \boldsymbol{u}_L \quad \text{and} \quad \partial_t^2 \boldsymbol{u}_T = \frac{\mu}{\rho}\nabla^2 \boldsymbol{u}_T. \tag{5.25}$$

From the structure of Eq. (5.25) the phase velocities unveils themselves as

$$c_L^2 = \frac{2\mu+\lambda}{\rho} = \frac{(1-\nu)}{(1-2\nu)(1+\nu)}\frac{E}{\rho} \quad \text{and} \quad c_T^2 = \frac{\mu}{\rho} = \frac{1}{2(1+\nu)}\frac{E}{\rho} \tag{5.26}$$

where the latter equality is obtained, by inserting of the found expressions for the Lamé parameters λ and μ in Eqs. (5.19). The longitudinal compression waves, moves with a greater velocity than the transverse shear waves. It can be shown by the ratio $\frac{c_T}{c_L}$ that the phase velocity difference is described as an inequality $2c_T^2 \leq c_L^2$.

It is often useful to express the equation of motion (without force $\boldsymbol{f}$) in terms of the phase velocities, which again is described by the material parameters. This will ensure a description of the material by mixed waves in contrary to distinctly separated longitudinal and transverse waves. By substitution of μ and λ in Eq. (5.21) with phase-velocities, it is seen that

$$\partial_t^2 \boldsymbol{u} = c_T^2 \nabla^2 \boldsymbol{u} + (c_L^2 - c_T^2)\boldsymbol{\nabla}(\boldsymbol{\nabla}\cdot\boldsymbol{u}) \tag{5.27a}$$
$$\partial_t u_i = c_T^2 \partial_k^2 u_i + (c_L^2 - c_T^2)\partial_i \partial_j u_j \tag{5.27b}$$

with stress tensor from eq. Eq. (5.15) as

$$\boldsymbol{\sigma} = \rho[c_T^2(\boldsymbol{\nabla}\boldsymbol{u} + (\boldsymbol{\nabla}\boldsymbol{u})^\intercal) + (c_L^2 - 2c_T^2)(\boldsymbol{\nabla}\cdot\boldsymbol{u})\,\mathbf{1}] \tag{5.28a}$$
$$\sigma_{ij} = \rho[c_T^2(\partial_i u_j + \partial_j u_i) + (c_L^2 - 2c_T^2)\partial_k u_k \delta_{ij}]. \tag{5.28b}$$

Evidently the equation of motion takes the compact form

$$\partial_t^2 \boldsymbol{u} = \frac{1}{\rho}\boldsymbol{\nabla}\cdot\boldsymbol{\sigma}. \tag{5.29}$$

This is the description of the stress tensor and Navier's equation of motion in elastic isotropic solids not being infinite. That is, the theoretical separation of longitudinal compression waves and transverse shear waves, builds upon an assumption of infinite solid materials of elastic nature. In reality finite materials are described by a mix of longitudinal and transverse waves, by the stress and equation of motion just

presented above in Eqs. Eq. (5.27) and Eq. (5.28).

Considering a time harmonic dependency of the displacement field $\boldsymbol{u}(\boldsymbol{r},t)$ (i.e. harmonic oscillations of displacement) the field is described as $\boldsymbol{u}(\boldsymbol{r},t) = \boldsymbol{u}(\boldsymbol{r})\mathrm{e}^{-i\omega t}$. It is thus seen that the time derivative of the displacement field is $\partial_t \boldsymbol{u}(\boldsymbol{r},t) = -i\omega$, which is then utilized to described the equation of motion described by phase velocities in Eq. (5.27) as

$$-\omega^2 \boldsymbol{u} = c_T^2 \nabla^2 \boldsymbol{u} + (c_L^2 - 2c_T^2).\boldsymbol{\nabla}(\boldsymbol{\nabla}\cdot\boldsymbol{u}) \tag{5.30}$$

Once again by a Helmholtz decomposition using Eq. (5.22) the time-harmonic equation of motion yields

$$-\omega^2(\boldsymbol{u}_L + \boldsymbol{u}_T) = c_L^2 \nabla^2 \boldsymbol{u}_L + c_T^2 \nabla^2 \boldsymbol{u}_T. \tag{5.31}$$

When separated into purely longitudinal and transverse parts becomes

$$\nabla^2 \boldsymbol{u}_L = -k_L^2 \boldsymbol{u}_L \quad \text{and} \quad \nabla^2 \boldsymbol{u}_T = -k_T^2 \boldsymbol{u}_T \tag{5.32}$$

with

$$k_L = \frac{\omega}{c_L} \quad \text{and} \quad k_T = \frac{\omega}{c_T}. \tag{5.33}$$

which is the Helmholtz's equation with wavenumbers k_L and k_T for longitudinal and transverse components, respectively.

Chapter 6

Computational tasks in COMSOL

6.1 The finite element method

6.1.1 Strong and weak formulation

The finite element method (FEM) is a numerical way of solving both ordinary differential equations (ODE) and partial differential equations (PDE). COMSOL is a numerical FEM software, which is used to simulate the scenarios investigated in this project[7]. We will now look into the theory behind implementation of FEM in COMSOL by following the note by [8, Bruus]. FEM is a method where a domain is discretized into a huge number of triangular mesh cells of finite sizes in the domain as sketched in Fig. 6.1. The benefit of these finite elements is that local approximations of the problem can be solved for and pieced together. FEM is a very useful method in the way that the strong representation

$$\boldsymbol{\nabla}\cdot\boldsymbol{J} - \boldsymbol{F} = \boldsymbol{0} \tag{6.1}$$

can be approximated by a so-called weak formulation. Here $\boldsymbol{J}$ is a generalized flux tensor, which is driven by the generalized force $\boldsymbol{F}$.

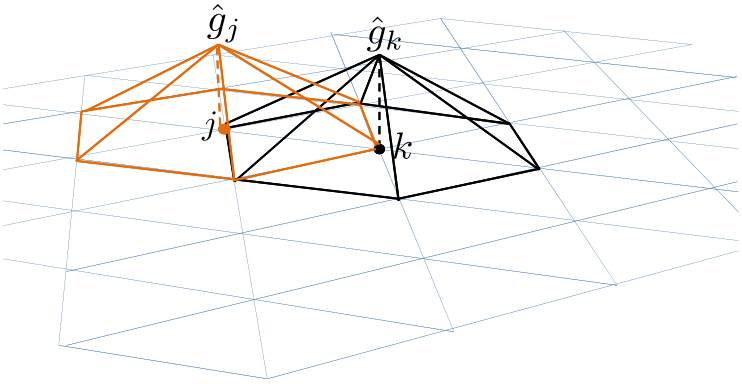

Figure 6.1: Finite element method: 2D depiction of two overlapping basis-functions $\hat{g}_k$ and $\hat{g}_j$ in the domain Ω centered over node k and j, respectively. The basis functions are spanned by the neighboring nodes to node k and j. Note that the tent-shape of these basis functions is due to linear (first order) polynomials describing the decrease from value 1 to 0 on the boundary of the cells.

A given mesh cell centered on a node k defines the basis function $\hat{g}_k$, where the basis function is spanned by neighboring mesh vertices. $\hat{g}_k$ is defined such that it has the value of 1 on node k, whereas $\hat{g}_j$ has the value 1 on node j. The values of these basis functions is continuously decreasing to become zero everywhere on the boundary of the basis-function cell and at the neighboring nodes. Having a large number of basis functions sharing two triangular mesh elements such that overlaps are present (see Fig. 6.1), makes up a set of all basis functions constituting a non-orthogonal basis. This is allowing any function $g(\boldsymbol{r})$ to be approximated by the linear combination

$$g(\boldsymbol{r}) \approx \sum_k C_k \, \hat{g}_k(\boldsymbol{r}). \tag{6.2}$$

where $\hat{g}_k$ are basis functions for node k, and coefficients C_k that approximates the arbitrary function $g(\boldsymbol{r})$. The approximation introduces a non-zero defect $d(\boldsymbol{r})$ such that the strong form Eq. (6.1), where the current $\boldsymbol{J}$ is dependent on the basis functions, then becomes

$$\boldsymbol{\nabla} \cdot \boldsymbol{J}[g(\boldsymbol{r})] - \boldsymbol{F}(\boldsymbol{r}) = d(\boldsymbol{r}) \tag{6.3}$$

The strong form requires the terms in the PDE to be well-defined for all points in the problem at hand, yielding function spaces of infinite proportions. In contrary

for the weak form, it is enough to require that

$$\int_\Omega \hat{g}_m(\boldsymbol{r})[\boldsymbol{\nabla}\cdot\boldsymbol{J}[g(\boldsymbol{r})] - \boldsymbol{F}(\boldsymbol{r})]\mathrm{d}V = 0, \quad \text{for all} \quad m \in \mathbb{Z} \tag{6.4}$$

such that the equality holds in an integral sense; that is, the projection of the defect $d(\boldsymbol{r})$ on each basis function becomes zero. Eq. (6.4) is indeed the weak form of the boundary value problem.

6.1.2 Linear equations in COMSOL

COMSOL is solving and outputting solutions for systems of linear equations $\boldsymbol{Ax} = \boldsymbol{g}$. Splitting up the integral Eq. (6.4) to the form

$$\int_\Omega \hat{g}_m(\boldsymbol{r})\boldsymbol{\nabla}\cdot\boldsymbol{J}[g(\boldsymbol{r})]\,\mathrm{d}V = \int_\Omega \hat{g}_m(\boldsymbol{r})\boldsymbol{F}(\boldsymbol{r})\,\mathrm{d}V \tag{6.5}$$

Introducing a system matrix with a linear current operator $\boldsymbol{J}[g(\boldsymbol{r})]$

$$A_{mk} = \int_\Omega \hat{g}_m(\boldsymbol{r})\boldsymbol{\nabla}\cdot\boldsymbol{J}[\hat{g}_k(\boldsymbol{r})]\,\mathrm{d}V \tag{6.6}$$

which is often referred to as the stiffness matrix, due to historical applications of FEM in structural mechanics. Moreover, the force load vector is

$$F_m = \int_\Omega \hat{g}_m(\boldsymbol{r})\boldsymbol{F}(\boldsymbol{r})\,\mathrm{d}V. \tag{6.7}$$

So forth, the weak form of the boundary value problem Eq. (6.4), can be rewritten in terms of a matrix problem

$$A_{mk}C_k = F_m \tag{6.8}$$

where C_k evidently is the solution coefficients obtained by classical matrix inversion, which exists for each field.
The weak form of the boundary value problem is a volume integral over the domain Ω. To identify the explicit contributions from the bulk and boundary, Green's first identity Eq. (B.9) is used on the divergence term in Eq. (6.4) to obtain

$$\oint_{\partial\Omega} \hat{g}_m(\boldsymbol{r})\boldsymbol{n}\cdot\boldsymbol{J}\,\mathrm{d}A + \int_\Omega [(-\boldsymbol{\nabla}\hat{g}_m(\boldsymbol{r}))\cdot\boldsymbol{J} - \hat{g}_m(\boldsymbol{r})\boldsymbol{F}(\boldsymbol{r})]\,\mathrm{d}V = 0 \tag{6.9}$$

which then can be utilized to construct the model problem for the boundary and bulk in COMSOL.

6.2 Theoretical model of acoustofluidic PMMA device

In this thesis we will model an acoustofluidic PMMA device by a fluid-solid coupling introduced with the proper boundary conditions obtained from literature by [9, Bruus]. The device contains water in a micro-fluidic channel of width W_F, height H_F and length L_F, carved in PMMA with height H_S, width W_S and length L_S for different dimensions of the device, given in table G.3. After the micro-fluidic channel has been carved, using precision mechanical machining, a lid of height H_{lid} is bonded as a PMMA cover film. A piezoelectric transducer is placed either on top or bottom (see Fig. 6.2) of the device, the transducer is carved in the middle leaving a finite gap of width ΔW. The transducer actuates the device by a push-pull actuation at MHz frequencies, creating a standing wave in the channel at the right frequencies. This acoustophoresis is used to control, sort and fixate biological cells inside the channel. A 3D view of the device is given in Fig. G.2, where a cross-sectional view of the work plane is given in Fig. 6.2. Due to high symmetry in the length-direction the model is simplified to the 2D work plane. The model is constructed assuming constant temperature and stop-flow condition.

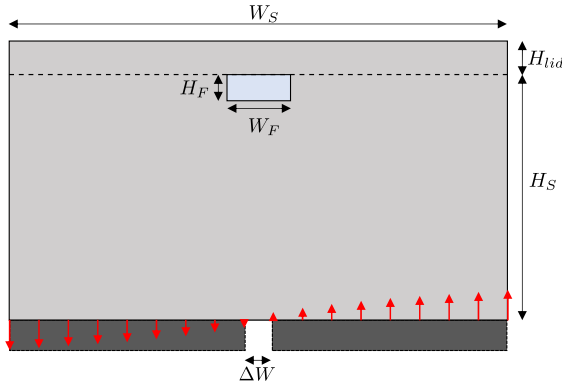

Figure 6.2: Cross-sectional view of the work plane in Fig. G.2, showing the dimensions of the PMMA device with fluid channel (light blue) surrounded by PMMA (grey) actuated at the bottom (red arrows - not to scale), with a piezoelectric transducer (dark grey).

The model used in this thesis is based on time harmonic fields $f(\boldsymbol{r}, t) = f(\boldsymbol{r})\mathrm{e}^{-i\omega t}$ and the only two fields of interest are the first order pressure field p and the displacement field $\boldsymbol{u}$. Using the weak formulation in `COMSOL-Multiphysics`, the fields must be governed by equations similar to that of Eq. (6.1). Fortunately the first

order acoustic pressure field is governed by Helmholtz's equation

$$\boldsymbol{\nabla} \cdot (\boldsymbol{\nabla} p) + k^2 p = 0 \tag{6.10a}$$

as in Eq. (3.13), and the displacement field is governed by

$$\boldsymbol{\nabla} \cdot \boldsymbol{\sigma} - \rho_s \partial_t^2 \boldsymbol{u} = \mathbf{0}, \tag{6.10b}$$

where the stress tensor $\boldsymbol{\sigma}$ is given in Eq. (5.28). From first order perturbation theory discussed in section 3.1, it was found that time derivatives takes the form $\partial_t \to -i\omega(1 + i\Gamma)$ as derived in and shown cf. Eq. (3.12). This damping occurs in the dynamics of the fluid and solid, which is to be coupled in one complete system. This means that the governing equations Eq. (6.10) takes the form

$$\boldsymbol{\nabla} \cdot \boldsymbol{\nabla} p - F_f = 0 \tag{6.11a}$$

$$\boldsymbol{\nabla} \cdot \boldsymbol{\sigma} - \boldsymbol{F}_s = \mathbf{0} \tag{6.11b}$$

with

$$F_f = -\frac{\omega^2}{c_f^2}(1 + i\Gamma_f)^2 p \quad \text{and} \quad \boldsymbol{F}_s = -\rho_s \omega^2 (1 + i\Gamma_s)^2 \boldsymbol{u} \tag{6.12}$$

6.2.1 Boundary conditions

The following assumptions that must be fulfilled at the boundary interfaces is a continuous velocity field across the interface, described as

$$\boldsymbol{n} \cdot \boldsymbol{v} = -\frac{i}{\rho_f \omega (1 + i\Gamma_f)^2} \boldsymbol{n} \cdot (\boldsymbol{\nabla} p), \tag{6.13a}$$

$$\boldsymbol{t} \cdot \boldsymbol{\sigma} \cdot \boldsymbol{n} = 0, \tag{6.13b}$$

given that the velocity is proportional to the pressure gradient as in Eq. (4.2). The tangent vector is denoted $\boldsymbol{t}$. Also the stress must be continuous across the boundary,

$$\boldsymbol{n} \cdot \boldsymbol{\sigma} \cdot \boldsymbol{n} = p \tag{6.14a}$$

$$\boldsymbol{t} \cdot \boldsymbol{\sigma} \cdot \boldsymbol{n} = 0 \tag{6.14b}$$

On the solid-air boundary, the normal of the stress $\boldsymbol{\sigma} \cdot \boldsymbol{n}$ is zero. That is, the surrounding air is assumed to be a vacuum, hence there is no stress originating from the ambient media. The solid-transducer boundary is actuated according to Fig. 6.2 with displacement $\boldsymbol{u} = \boldsymbol{d}_0 = d_0 \hat{\boldsymbol{e}}_z$. It is noted that the gap of width ΔW on this figure, is made to ensure an efficient push-pull effect of the actuation. On the

solid-fluid interface (i.e. seen from the solid) the stress normal to the surface is the (negative) pressure $-p\boldsymbol{n}$, since it is working against the solid. Finally, the boundary condition at the fluid-solid interface (i.e. as seen from the fluid) is coming from the inviscid first-order acoustic Navier-Stokes Eq. (3.7)

$$\rho_f \partial_t \boldsymbol{v} = -i\rho_f \omega \boldsymbol{v} = -\boldsymbol{\nabla} p$$

By coupling the velocity field in the fluid with the displacement field in the solid, then exactly at the boundary

$$\boldsymbol{v} = \partial_t \boldsymbol{u} = -i\omega \boldsymbol{u}$$

which implies

$$\boldsymbol{\nabla} p = \rho_f \omega^2 \boldsymbol{u}$$

. To distinguish between fluid and solid properties, the subscript f and s are used, respectively, in the following. Now the boundary conditions in mathematical form thus become

$$\begin{aligned}
&\text{solid-air :} && \boldsymbol{\sigma}_s \cdot \boldsymbol{n} = \boldsymbol{0} && \text{(6.16a)}\\
&\text{solid-transducer :} && \boldsymbol{u} = d(y)\hat{\boldsymbol{e}}_z && \text{(6.16b)}\\
&\text{solid-fluid :} && \boldsymbol{\sigma}_s \cdot \boldsymbol{n} = -p\boldsymbol{n} && \text{(6.16c)}\\
&\text{fluid-solid :} && \boldsymbol{n} \cdot \boldsymbol{\nabla} p = \rho_f \omega^2 \boldsymbol{n} \cdot \boldsymbol{u} && \text{(6.16d)}
\end{aligned}$$

where the first-mentioned domain is where the boundary conditions are seen from (e.g. solid-air is the boundary condition as seen from the air). The solid-transducer condition is modelled with the odd function

$$d(y) = d_0 \tanh\left(20\frac{y}{W_S}\right), \tag{6.17}$$

where the factor of 20 account for the finite gap ΔW between the two transducers (see Fig. 6.2), which is in the order of $\frac{1}{20}W_S$. This function ensures that the displacement is continuous across the solid-transducer interface. For implementation in COMSOL see appendix C.

6.3 Verification and validation

6.3.1 Conceptual agreement

To verify our COMSOL model, we study a well-known problem; the anti-symmetric actuation of infinite hard walls (see chapter 4).

To model infinite hard walls we use the same model as in section 6.2, but without the finite solid. Instead we impose the zero flux boundary condition on top and bottom and the anti-symmetric actuation at $\pm L$. Since the walls are assumed infinite hard and the actuating amplitude d_0 is small, compared to the dimension of the channel, we set the boundary condition $v(\pm L) = \pm\omega d_0$. This is implemented as Eq. (6.16b), but at the side-walls instead of the bottom.

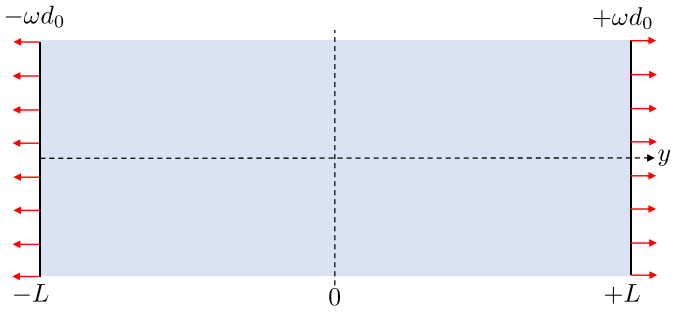

Figure 6.3: Simple configuration for anti-symmetric actuation of infinite hard walls, with high symmetry. The walls are actuated in counterphase with an amplitude ωd_0, the width of the channel is $2L = 375\,\mu\text{m}$.

The boundary conditions for the given problem are

$$\partial_y p = \begin{cases} -\rho_0\omega^2(1+i\Gamma_f)^2 d_0 & \text{for} \quad y = -L \\ +\rho_0\omega^2(1+i\Gamma_f)^2 d_0 & \text{for} \quad y = +L \end{cases} \tag{6.18}$$

Hard walls means that the normal velocity component in the fluid will be zero at the interface between the fluid and the walls

$$\boldsymbol{n} \cdot \boldsymbol{v} = 0 \tag{6.19}$$

or in terms of the pressure

$$\boldsymbol{n} \cdot \boldsymbol{\nabla} p = 0 \tag{6.20}$$

which is exactly the zero flux condition in this case because our modelled flux is $\boldsymbol{\nabla} p_1$.

The acoustic theory predicts a stationary standing wave for the velocity as in Eq. (4.8) with the maximum amplitude $|v|_{\max} \approx \frac{\omega_n d_0}{n\pi\Gamma} = \frac{d_0}{\Gamma L} c_0$ at frequency $f = \frac{c_0}{2L} = 3.99\,\mathrm{MHz}$ for $n = 1$ given in sec. 4.1. For the parameters given in table G.1 the maximum velocity amplitude is $|v|^{\text{theory}}_{\max} = 19.956\,\mathrm{cm\,s^{-1}}$ and the COMSOL model yields $|v|^{\text{model}}_{\max} = 19.957\,\mathrm{cm\,s^{-1}}$ an relative error of $\sim 10^{-5}$. This small error appears in the sense that the analytically line plot in Fig. 6.4 follows the numerical solution. Parameters used for this model are given in table G.1.

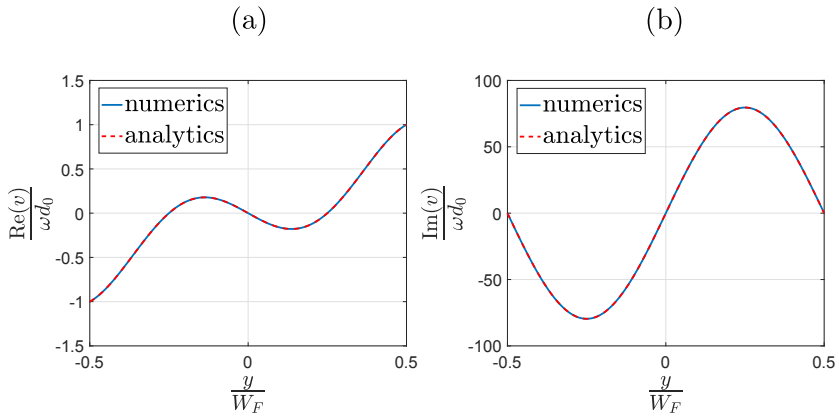

Figure 6.4: Line plot of the velocity field inside the fluid channel, with width $W_F = 2L = 375\,\mu\mathrm{m}$ under the hard-walls condition actuated at the eigenfrequency $f = 3.99\,\mathrm{MHz}$. (a) Real part obeying the oscillatory walls. (b) Imaginary part obeying the hard-walls condition, where the resonance yields eighty times larger amplitude.

In the following we are also using COMSOL to model the solid displacement field of a cantilever as described by [10, Bruus]. To verify our model we make use of the well-known theoretical solution to the cantilevered beam fixed at one end. The cantilever will have the length $L = 70\,\mathrm{mm}$ and height $H = 1\,\mathrm{mm}$ and the material is Pyrex 7740 borosilicate glass, with parameters given in table G.1.

The governing equations in this model will be the same as in section 6.2, which means that the no-stress condition imposed on all boundaries is equivalent to zero flux, since the modelled flux is the stress. To see if there exist an eigenfrequency, predicted from theory, the cantilever is excited at the clamped end. This excitement is modelled as a purely harmonic transverse displacement with amplitude $d_0 = 0.1\,\mathrm{nm}$. For the given case the natural frequencies of vibrations is given by [11, Landau & Lifshitz]

$$f_n = \frac{\xi_n^2}{2\pi\sqrt{12(1-\nu^2)}}\sqrt{\frac{E}{\rho}}\frac{H}{L^2}, \qquad n \in \mathbb{N}, \tag{6.21}$$

where ξ_n are solutions to $\cosh(\xi_n)\cos(\xi_n) + 1 = 0$. These frequencies is related to the bending moment $M = -EI\kappa$, where I is the second order moment depending on the cross-sectional area of the beam and κ is the local radii of curvature.

The first four eigenfrequencies are

$$f_1 = 0.178\,\text{kHz}, \quad f_2 = 1.12\,\text{kHz}, \quad f_3 = 3.13\,\text{kHz}, \quad f_4 = 6.14\,\text{kHz}, \quad f_5 = 10.2\,\text{kHz}.$$

To compare with the model a frequency sweep in the interval from 0.13 to 11 kHz is computed and for each frequency the glass is probed with the average transverse displacement squared $|\boldsymbol{u}_T|^2$.

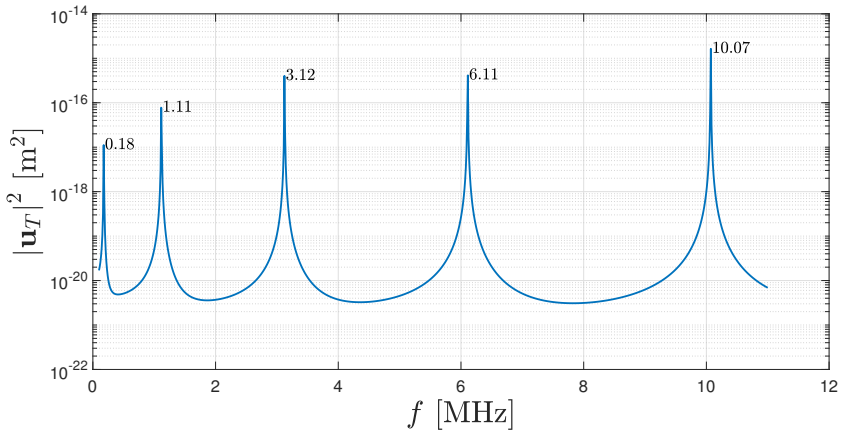

Figure 6.5: Frequency sweep, searching for the eigenfrequencies of a clambed cantilever, plotted on a logarithmic scale making it easier to see the peaks.

Comparing Fig. 6.5 shows good agreement with the theoretical values, with an error of ∼5%. The theoretical solutions also requires that $H \ll L$, so making the cantilever even longer would minimize the error. The hard-wall fluid channel and the cantilevered beam shows good agreement with the theory, and our COMSOL model is evidently verified by the analytical comparison to modelled numerics.

6.3.2 Mesh-convergence analysis

In order to determine the accuracy of the results - yet to be presented - a mesh convergence analysis is to be carried out. As described in section 6.1 and depicted in Fig. 6.1 a domain of interest in a given investigation is discretized by finite triangular

mesh elements. The coarseness of a mesh is a crucial factor in pursuit of a solution of sufficient accuracy. A relative convergence parameter is defined as

$$C(g) = \sqrt{\frac{\int (g - g_{ref})^2 \, \mathrm{d}y\mathrm{d}z}{(\int g_{ref})^2 \, \mathrm{d}y\mathrm{d}z}} \tag{6.22}$$

where g is the solution for a given field, and g_{ref} is the best solution that can be obtained (i.e. the finest mesh). In this case g_{ref} corresponds to a mesh of 752,294 elements and 2,955,149 degrees of freedom (DOF), which was the finest solution that could be obtained with the available hardware[1]. In contrary the most coarse mesh consists of 19,194 elements and 76,119 DOF and can be seen depicted in Appendix F on Fig. F.1. By means of Eq. (6.22) a plot of how the solution g converges to a satisfactory level g_{ref} as a function of relative mesh size is shown below.

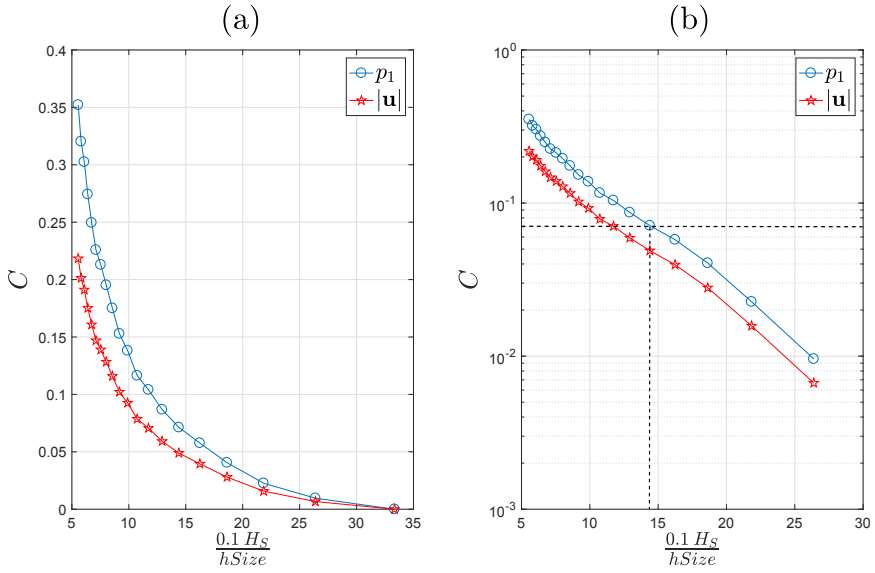

Figure 6.6: Mesh convergence analysis of the first order pressure and displacement fields p_1 and $|\boldsymbol{u}|$, respectively, carried out by a parametric sweep of the mesh size $hSize$ with COMSOL. The convergence plots are obtained using the computed values of C from Eq. (6.22) versus the relative mesh size parameter defined as $\frac{0.1H_S}{hSize}$. On fig (a) the convergence on standard axes is plotted, showing a exponential behavior, why (b) is a semi-logarithmic y-axis plot of the same fields. A threshold is chosen for an acceptable error of $\approx 7\%$ for the pressure field p_1 and $\approx 5\%$ for the displacement field (horizontal dashed line). This establish a value for the mesh size value $hSize = 10\,\mu\mathrm{m}$ or $\frac{0.1H_S}{hSize} \approx 15$ (vertical dashed line).

[1]We used a WorkStation running Windows 7 OS with 24 GB RAM for the computations.

where it is seen that the computed convergence of the field, follows the same trend converging asymptotically towards zero. Note however, that on the Fig. 6.6 C converges completely to 0, because the solution and reference is equal, $g = g_{ref}$ which is not the case in reality. However g_{ref} is a manually set baseline or reference for the solution in this case. From this point the simulations carried out in this thesis, are based on this convergence analysis giving us a value for the mesh-element scale at $hSize = 0.01\ H_S$, which scales with solid height H_S. The threshold is chosen as an optimum value with regards to the trade-off between computational time and accuracy of the solutions. The reduce this computational time during our investigations, we have establish a routine as follows:

1. A semi-coarse mesh is used to sweep in the interval from 1 to 2 MHz with $hSize = 0.05 H_S$ to screen for eigenfrequencies.
2. A zoom on the chosen eigenfrequency is conducted with $hSize = 10\,\mu\text{m}$ finding a single value for the eigenfrequency.
3. Further investigations of this eigenfrequency is conducted with use of $hSize = 10\,\mu\text{m}$

.

Chapter 7

Coupled resonances

7.1 Water

Before analyzing the soft-solid and liquid interplay, it is rather important to see how the liquid yields to the working actuation. To model water alone we use the hard-wall conditions, as in sec. 6.3.1, this means that the solid parameters have no influence and the eigenfrequencies at hand will be the liquid yielding to the hard walls.

To establish connections between results, the same parameters and geometry as in sec. 6.2 are used, which is that of Device A given in table G.3 and G.1.

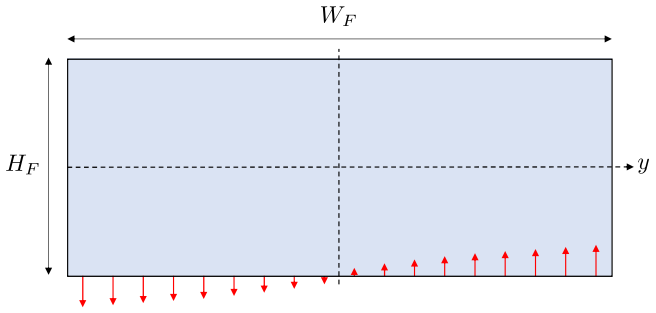

Figure 7.1: Schematics showing the actuation (red arrows - not to scale) using the hard-wall condition, for the fluid channel with dimensions given in table G.3.

Searching for the eigenfrequencies the liquid domain is probed with the averaged acoustic energy density as in Eq. (4.18), since eigenfrequencies will yield the Lorentzian shape given in Eq. (4.13). Evidently a parametric sweep can be computed around the frequencies of interest, in this case 1 to 3 MHz.

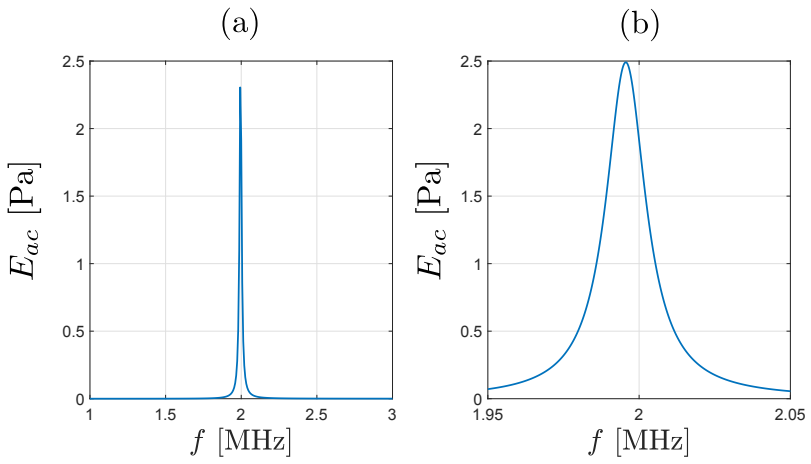

Figure 7.2: (a) Frequency sweep searching for water's eigenfrequency in the interval from 1 to 3 MHz. (b) Zoom of the given eigenfrequency 1.996 MHz at a higher resolution with a Q-factor of 125, using more steps.

From Fig. 7.2 it is clear that if we actuate the device with infinite hard walls around $f = 2\,\text{MHz}$, more precise 1.996 MHz matching the acoustic wavelength of $\lambda = 2W_F = 750\,\mu\text{m}$, the water will resonate. This eigenfrequency yields a pressure of $\sim$0.15 MPa and the symmetric surface around $y = 0$ is evidence of a standing half wave, see Fig. 7.3. This frequency will be referred to, as the eigenfrequency for water.

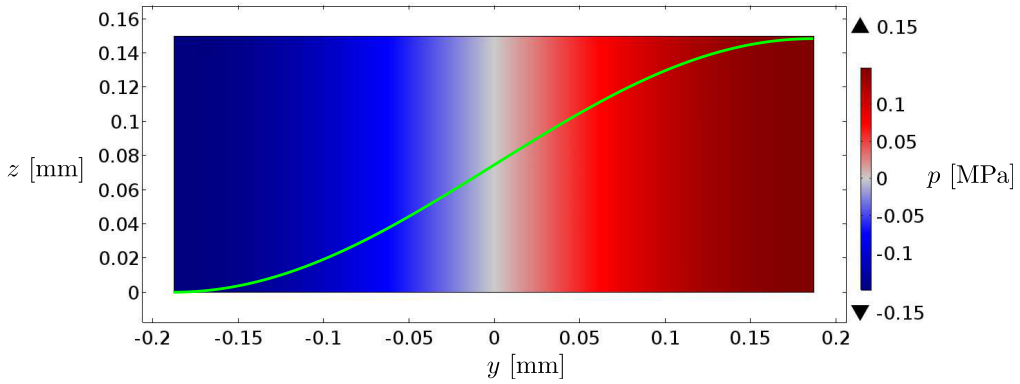

Figure 7.3: (a) Surface plot of the pressure in the fluid channel at the eigenfrequency 1.996 MHz yielding a pressure of magnitude $\sim$0.15 MPa due to the hard-wall condition. As the color plot indicates it goes symmetrically from -0.15 MPa to $+0.15$ MPa. The green line indicates the pressure profile evaluated on the horizontal cutline $z = H_F/2$.

7.2 Silicon-water

In real life the walls are not infinitely hard, that is why the whole system must be considered. The Piezoelectric transducer will also induce a strain in the solid and evidently both the solid and fluid will begin to resonate at certain frequencies. The solid will begin to wobble and so will the walls at the fluid channel, causing a stress on the water.

To illustrate this coupling we investigate how the fluid-solid model yields to certain frequencies by computing a frequency sweep as in Fig. 7.2, using device A, with dimensions given in table G.3. Since our model builds on the assumption that the solid is isotropic, we must however consider Silicon as isotropic. That is why we use Young's modulus and Poisson's ratio for a certain crystal direction, in this case the $\langle 110 \rangle$-direction. As well for the transverse and longitudinal speeds of sound. The parameters used to model the Silicon are given in table G.1.

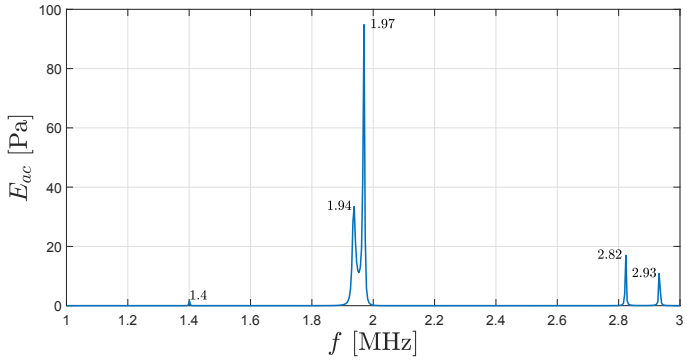

Figure 7.4: Frequency sweep searching for the eigenfrequencies for the coupled system Silicon-water using device A. For each step in frequency the acoustic energy is probed. The values for the eigenfrequencies is indicated above each peak.

In Fig. 7.4 the two largest energies are very close to that of the hard-wall given in Fig. 7.2. Further investigation of the frequency 1.97 MHz shows that the pressure inside the fluid channel takes the same form as for water, see Fig. 7.5. The deformation of the device seems to be antisymmetric at $y = 0$, having the largest deformation in the upper corners and at the fluid-solid interface. Evidently the push-pull actuation becomes effective at 1.97 MHz, with a maximum displacement of 10.9 nm hundred times larger than the actuation amplitude $d_0 = 0.1$ nm.

The similarity between the two eigen-frequencies is evidence of water's influence. This means that for relative hard solids ($\geq 2000\,\mathrm{kg\,m^{-3}}$) with high acoustic impedance, the eigenfrequency of water dominates.

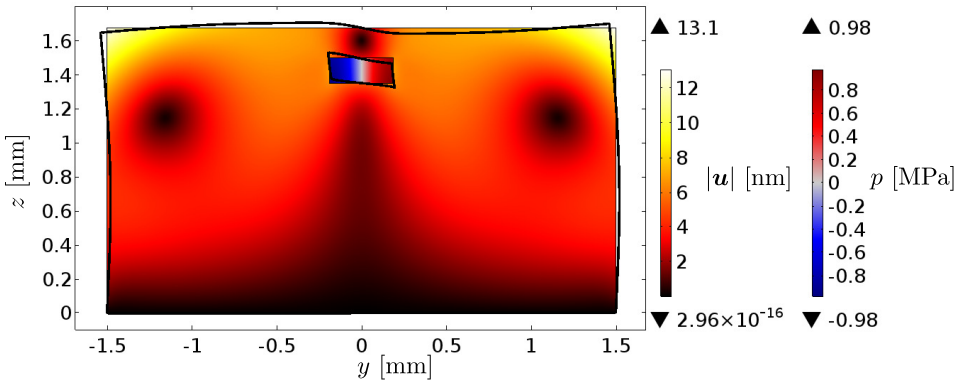

Figure 7.5: Surface plot of the absolute displacement in the solid and the pressure inside the fluid channel, actuated at 1.97 MHz. The black line around the device illustrates the deformation of the device (scaled with a factor of 2×10^4). The dimensions is that of device A given in table G.3. The black triangles next to the color bars are showing the max/min values of the quantity the respective color-bar is representing.

7.3 PMMA-water

Instead of Silicon we introduce the polymer Poly(methyl methacrylate) (PMMA) as proposed in [12]. However PMMA is rather soft, having almost the same density as water and low acoustic impedance. This introduces a strong coupling between the fluid channel and the surrounding solid. The first step to visualize this coupling is to do a frequency sweep.

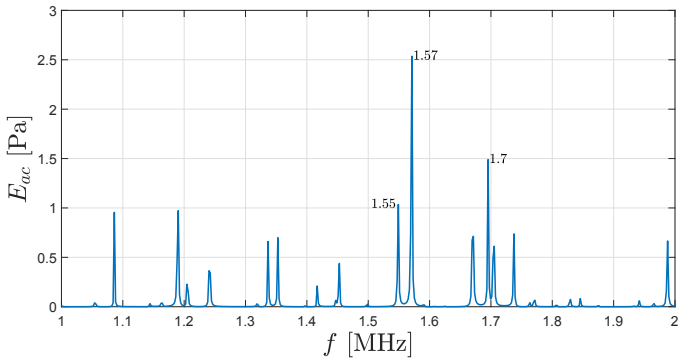

Figure 7.6: Frequency sweep searching for the eigenfrequencies for the coupled system PMMA-water, for device A. The three eigenfrequencies with the highest acoustic energy density is indicated above each peak.

Searching for the eigenfrequencies in the Silicon-water device, we found three, with a acoustic energy density of ∼100 Pa. Coupling water and PMMA yields thirty-four peaks, due to the PMMA-water similarities. Analyzing all eigenfrequencies for such a system is comprehensive and that is why we only consider the three frequencies with the highest energies. Although the energy in the PMMA device is much less than that of Silicon-water, the pressure and displacement is the same order of magnitude, see Fig. 7.7. The frequency domain from 1 to 2 MHz is chosen, since the experimental measurements are preferable in this interval.

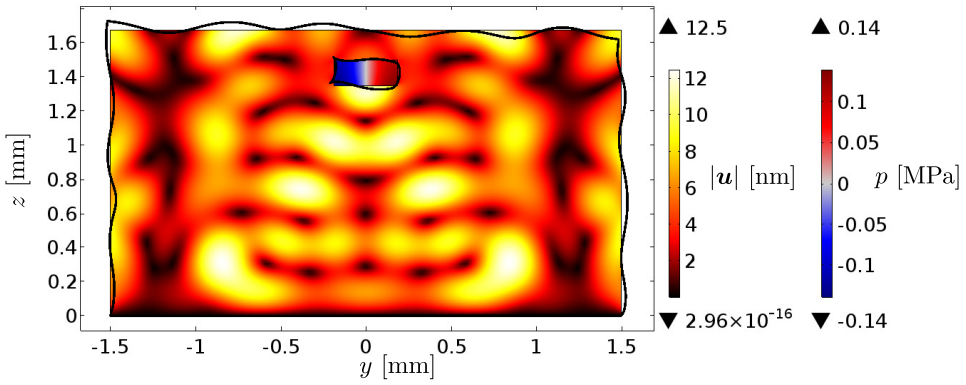

Figure 7.7: Surface plot of the absolute displacement in the solid and the pressure inside the fluid channel, actuated at 1.57 MHz. The black line around the device illustrates the deformation of the device (scaled with a factor of 1×10^4). The dimensions is that of device A given in table G.3.

Evidently the coupling in the PMMA-water device is rather complex than that of Silicon-water and the distinct water resonance around 2 MHz does not appear to be the largest as in Silicon. Coupling low acoustic impedance solids with water thus makes the system complex and here the model in section 6.2 must be appreciated to predict the outcome.

Chapter 8

Parametric studies

In cooperation with the Swedish bio-analytic company `AcouSort`, we have performed parametric studies of the PMMA device, based on the theory from previous chapters. The device is produced by the lab-on-a-chip company `Microfluidic ChipShop`. The dimensions of the different chips are given in table G.3.

To characterize the different devices we follow a standard procedure, as follows

(i) A frequency sweep in the interval from 1 to 2 MHz is studied. The frequency with the highest energy is taken out to further investigation.

(ii) If the frequency with the highest energy yields a half-wave resonance pressure wave in the fluid channel, then the radiation forces are analyzed. If not then the frequency with the second highest energy is analyzed etc.

(iii) If the net acoustic radiation forces point towards the center of the fluid channel then the frequency is rated as the best for the given device. If not then (ii) is conducted with the frequency yielding the second highest energy.

for each device the procedure is performed.

8.1 Top- and bottom-actuated acoustofluidic devices

Accordingly with the work procedure stated above, we found that the best geometric configuration of the acoustic devices actuated from the top is device C with dimensions given in G.3, and an acoustic energy density of 17.0 Pa at frequency 1.39 MHz. The bottom actuated device, yielding the best results is the geometric configuration

of device B, with acoustic energy density 5.36 Pa at frequency 1.63 MHz. These two candidates are from here on denoted B^{bot} and C^{top}, indicating the geometric configuration and actuation by a superscript. The conducted simulations of devices A, B and D with other geometric configurations for the top- and bottom-actuations are shown in Appendix H Fig. H.2 and Fig. H.3, respectively.

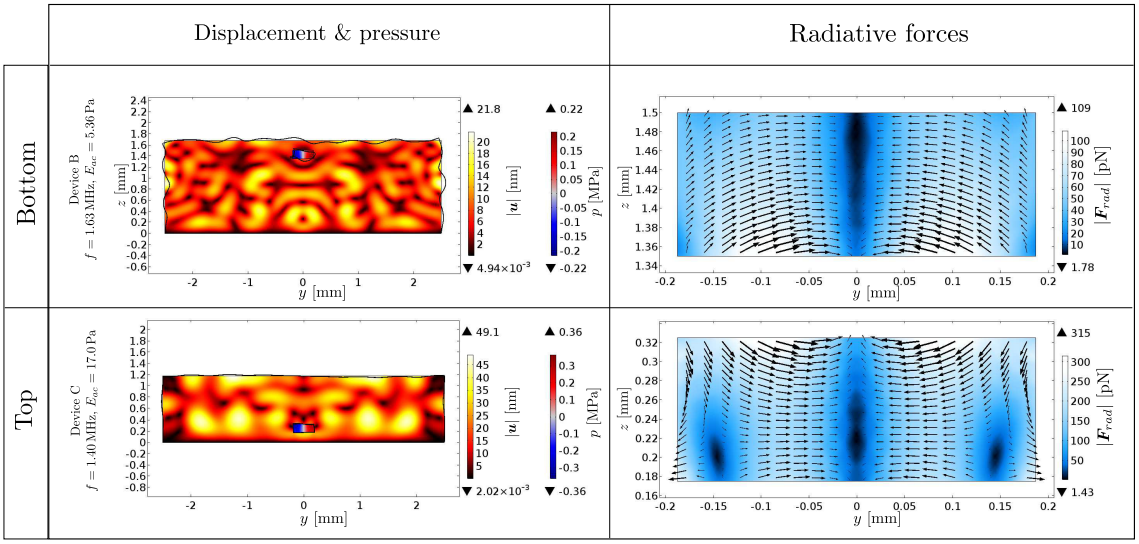

Figure 8.1: Graphical depiction of displacement, pressure and radiation forces of the best geometrical configurations for top- and bottom-actuation. On the top row the chosen candidate B^{bot} is shown and on bottom row the candidate, C^{top}. The left panel shows the displacement of the solid and the pressure inside the channel with corresponding explanatory color-bars for displacement and pressure, respectively. The line around the devices, is indicating the deformation of the PMMA at the stated frequencies scaled with a factor 2×10^4. The right panel shows forces and their directions. Note that the black triangle above/below each color-bar is giving the max/min value of the quantity it represents.

It is seen how the displacement of the PMMA domain is a somewhat random though symmetric wobble creating half-wave resonance at the stated frequencies. In other words, the whole system is wobbling thus creating the acoustic eigenmodes, at which we find resonances for the water in the microchannel. The whole device is displaced by the actuation, but does not resemble the actuation symmetry in any way. In contrary it is shown in Fig. 7.5 that displacement of higher density materials with hard walls follows the actuation, leading to a resonance close to that of water accordingly with Fig. 7.2. This is seen as the outer-wall displacement directly follows the push-pull actuation. Evidently the eigenfrequencies of PMMA systems or

similar elastic materials will be completely different. The displacement of candidate B^{bot} is also seen to be more pronounced than for C^{top}, as they are scaled by the same factor of 2×10^4.

The eigenmodes of the systems, creating half-wave resonances lead to an acoustic radiation force which can be utilized to confine particles in the local zero-pressure node(s). This is depicted as a surface color plot showing the local magnitude of forces in color with directions shown as arrows. By looking at the resulting force fields for both candidates B^{bot} and C^{top}, it is seen that the acoustic fields creates a force pointing towards the channel-center. The candidate B^{bot} is showing a nice and pretty uniform force field, with only a zero-force field mid-channel as wanted. The acoustic radiation force is maxing at 109 pN. Furthermore it is seen that the forces especially in the bottom and sides of the channel is having a component lifting the particle upwards. This is also a desired effect, as it compensates for the gravitational force, which is dragging the particle down in the bottom of the channel.

It is noted that the force field of C^{top} contains two zero-force points, symmetrically located around $y = \pm 15$mm, which potentially could lead to unwanted effects around those points, making particles able to escape the acoustic trapping. The argument to choose this candidate is the huge radiation force maxing at 315 pN. The ability to control and trap particles by the acoustic radiation forces is investigated further in the next section 8.2. This investigation is including the magnitudes of the different acting forces and their mutual interaction.

8.2 Acting forces and particle focusing

Given the right conditions, matter can be confined in a fluid due to the radiation forces, which exactly is the effect of acoustophoresis. This concept is utilized in different environments, in this case the fluid channel. The wanted effect is to focus particles in the center of the fluid channel, which can be accomplished by forces pointing towards the center where the zero force or pressure nodal plane is located as seen in Fig. 8.1.

To get a feeling for the working time scale, we compute the time it takes for a particle to travel from top to bottom of the channel. In the following, we use particles of radius $a = 10\,\mu$m. Assuming no or very little acceleration in the system $F = ma \approx 0$, and using the expression for buoyancy compensated gravitational force Eq. (4.26) and Stokes' drag Eq. (4.27) we have that the sum of 1D forces (in

z-direction) vanish $F_g^{comp} - F_d = 0$ or $F_g^{comp} = F_d$, which is

$$\frac{4}{3}\pi\rho_f(\tilde{\rho}-1)a^3 g = 6\pi\eta a v_z \tag{8.1}$$

where the velocity can be expressed in terms of distance and time as $v_z = H_F/t$, where t is the time it takes the beads to travel from top to bottom. Thus by inserting the values (seen in Table G.1) in the equation and solving for the time t we get the time t_g it takes for the gravity to pull one particle from top to bottom of the channel, as

$$t_g = \frac{9}{2}\frac{\pi\eta H_F}{\rho_f(\tilde{\rho}-1)a^2 g} = 36.34\text{s}. \tag{8.2}$$

Which is seen to be a rather slow effect originating from the combined and oppositely working forces F_g^{comp} and F_d. To relate this time and the acting forces, we will also look at the effect of the radiation force, and the time it takes to get particles confined in the zero force plane in the middle of the channel. The radiation force is stated in Eq. (4.23) and acts on particles as also indicated by the force fields of the chosen candidates B^{bot} and C^{top} as seen in Fig. 8.1. If we assume that the found acoustic eigen-frequencies for both candidates is exactly half waves fitting in the dimension W_F of the channel, we can write that $W_F = \lambda/2$ or $\lambda = 2W_F$. From previous studies in acoustofluidics, it follows that the time it takes for a particle to move from an initial position $y(0)$ to a final position $y(t)$ is given by combining and rearranging Eq. (4.25a) and Eq. (4.27), to yield

$$t_{rad} = \frac{9\eta}{4\Phi_{ps}(k_y a)^2 E_{ac}} \ln\left(\frac{\tan[k_y y(t)]}{\tan[k_y y(0)]}\right) \tag{8.3}$$

where $\Phi_{ps} = 0.328$ is the acoustic polystyrene-water coefficient [13], used for further analysis. This can be used to evaluate the time it should take to focus the particles. Thus a plot of the spatial position, as a function of time, can give an indication about other relevant parameters, such as the acoustic force density or energy.

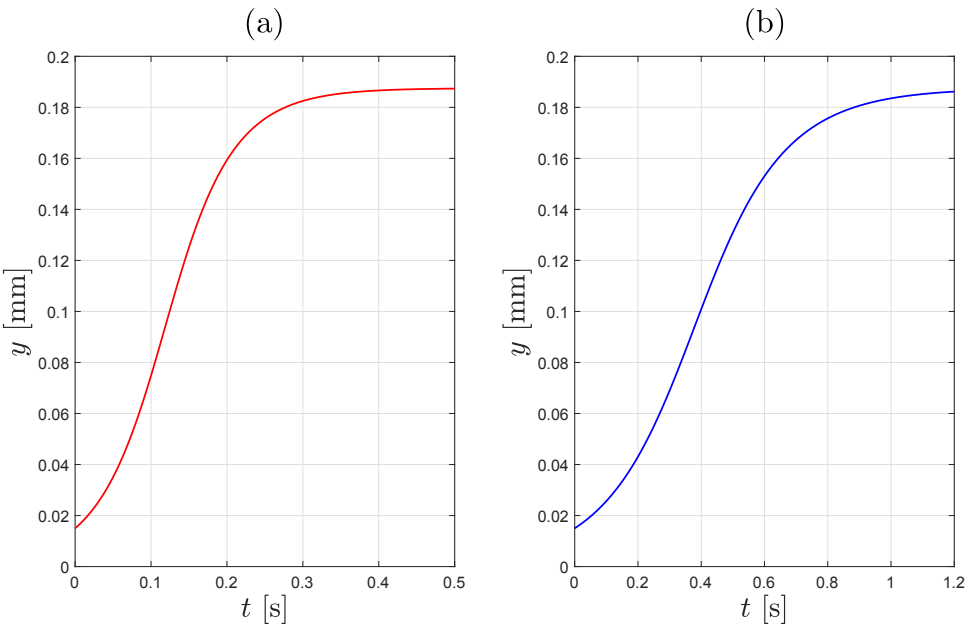

Figure 8.2: Plot of the acoustic radiation force F_{rad} and their corresponding time scales t with $a = 10\,\mu\text{m}$ particles for different channel positions y by means of Eq. (8.3). The initial position of the particles is $y(0) = 15\,\mu\text{m}$ from the channel wall until the micro beads comes to a rest at the pressure nodal plane mid-channel at $y(t) \approx 0.1875\,\mu\text{m}$. Candidate C^{top} plotted on (a) is focused after time $\approx 0.5\,\text{s}$ and candidate B^{bot} is plotted on (b) and focused after $\approx 1\,\text{s}$.

On the figure above it is seen how the to forces focusing a particle is behaving spatially, which is in great accordance with the forces on Fig. 8.3. The forces is greatest of magnitude on the middle, confirmed by the steeper slope on the graphs. It is also coherent, that candidate B^{bot} with a lower energy and thus smaller radiation force performs focusing less efficiently than candidate C^{top}.

We conduct simulations of the F_{rad} force field, to investigate the effectiveness of acoustophoresis of the chosen candidates.

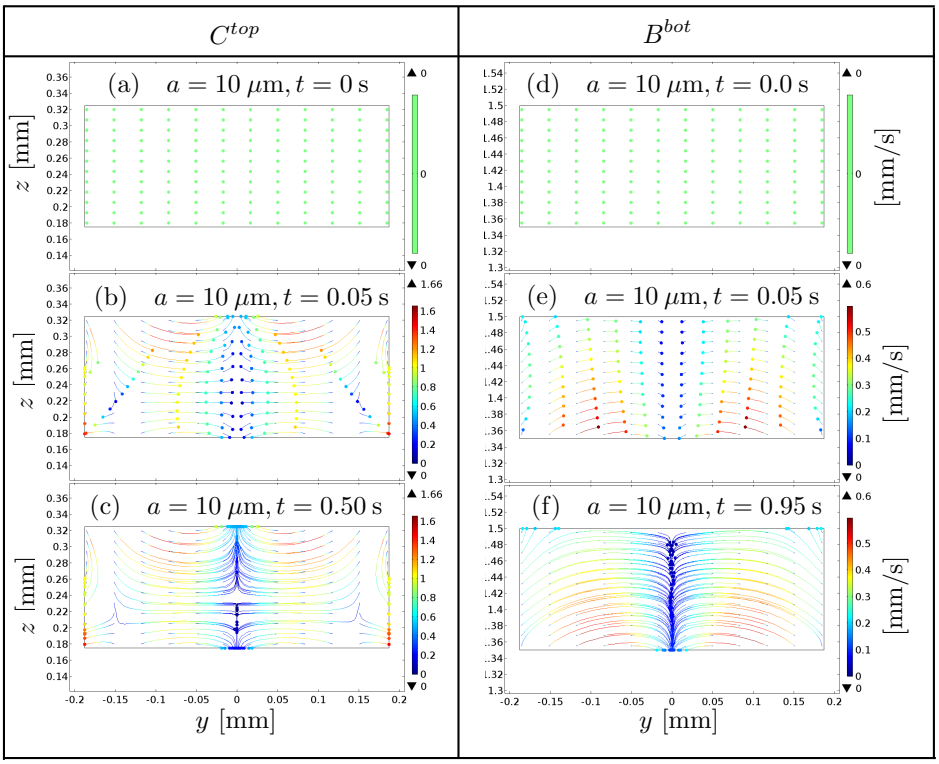

Figure 8.3: Simulation of particle trajectories due to radiation forces where the buoyancy compensated force F_g^{comp} and Stokes' drag force F_d are taken into account. The particle trajectories for the chosen candidates B^{bot} and C^{top} is shown at times t specified on (a) and (d) ($t = 0\,\text{s}$), showing the initial particle grid ($12 \times 12 = 144$ particles). On (b) and (e) at $t = 0.05\,\text{s}$ the movement of micro beads behaving in accordance with the force-fields depicted on Fig. 8.1. Finally (c) showing the particles at $t = 0.5\,\text{s}$, which is the time it takes to focus particles for candidate C^{top} and (f) shown at time $t = 0.95\,\text{s}$, which is the focusing time for candidate B^{bot}. The axes are measured in units of mm and color-bars show the corresponding local particle velocity in mm/s with an associated max/min value shown besides the black triangles of color-bars. As All the particle trajectories are computed for a particle radius $a = 10\,\mu\text{m}$. The simulation is done, such that once a particle gets in contact with a channel-wall, it will be stuck.

It is seen how the radiation force F_{rad} at time $t = 0\,\text{s}$ is a grid of the initial positions of the particles, for both top and bottom actuation. The candidate C^{top} which has the highest acoustic radiation force, does consequently also focus and confine the particles the fastest. The majority of the particle ensemble is released and thus

travelling in accordance with the force field as seen in Fig. 8.1, where the symmetrically located zero force points around $y = \pm 0.15\,\mathrm{mm}$ gives rise to an escape of the particles situated nearby, as expected. However, the beads travelling towards the center of the channel, as seen in Fig. 8.3, is moving rapidly due to the great radiation force and the rest of the particles are confined at $y = 0\,\mathrm{mm}$ at $t = 0.5\,\mathrm{s}$. The candidate B^{bot} has a more uniform force field, with only a zero-force point located in the middle of the microchannel. Evidently only few particles escape the acoustic radiation force, as seen in the simulation of this candidates B^{bot} particle trajectory simulation Fig. 8.3 (f). This is naturally a desired trade of this candidate, but is simultaneously a trade-off, as the magnitude of the radiation force is less than that of C^{top}. The smaller force magnitude yields a confinement of the whole ensemble of particles at $t = 0.95\,\mathrm{s}$, thus almost a factor 2 slower.

It is readily seen how the acoustic radiation force is by far the dominant force for both candidates, as the time it will take a particle to sink to the bottom $\sim$36 s is much greater than the time it takes to confine particles by radiation forces, which is also consolidated from the orders of magnitude of the forces $F_g = F_d \ll F_{rad}$.

With the characteristic length of the channel for the devices as $L_F = 40\,\mathrm{mm}$ the time it takes to completely focus the particles by radiation forces for the two candidates B^{bot} and C^{top}, can be translated into a critical flow rate. The focusing times are computed in Fig. 8.2 and confirmed in Fig. 8.3, by the `COMSOL` simulations of particle tracing.

For acoustophoresis to work properly, it must be that the focusing time, must be less than the time it takes a particle, to sink from top to bottom channel. Furthermore, these times must also be smaller than the time it takes a particle to flow through the entire channel. The time it takes for a particle to reach the bottom is much larger than the focusing time and also the the time it takes to flow through the channel, and thus gravity can be neglected. However the focusing time sets an upper limit for the flow rate. The critical flow rate for B^{bot} is

$$\dot{V} \approx 142\,\mu\mathrm{L\,min}^{-1} \quad \text{or} \quad \dot{V} \approx 237 \times 10^{-9}\,\mathrm{m^3\,s^{-1}} \tag{8.4}$$

where the critical flow rate is found by dividing the volume of the fluid channel with the focusing time. For candidate C^{top} the critical flow rate becomes

$$\dot{V} \approx 270\,\mu\mathrm{L\,min}^{-1} \quad \text{or} \quad \dot{V} \approx 450 \times 10^{-9}\,\mathrm{m^3\,s^{-1}}. \tag{8.5}$$

Thus the operating flow rate, should be less than these critical flow rates.

8.3 Uncertainty analysis of device candidates

Since that the eigenmodes presuppose a perfectly centered push-pull actuation with the exact geometric configurations as seen in table G.3, it is adjacent to investigate the uncertainties by fabrication of such devices. We have chosen to investigate the uncertainties of fabrication for the B^{bot} configuration, assuming that the other devices will follow the same tendency.

8.3.1 Transducer alignment

Doing the measurement on the acoustic device, one have to mount the piezoelectric transducer by hand. Doing so, means that the alignment is not perfect, probably off by approximately $\pm 0.5\,\text{mm}$. To analyze this effect, the solid-transducer condition Eq. (6.17) is modified as

$$d(y) = d_0 \tanh\left(20\frac{y - y_0}{W_S}\right), \tag{8.6}$$

which is just equivalent to an off-center transducer. Computing a parametric sweep in the parameter y_0 from $-0.5\,\text{mm}$ to $+0.5\,\text{mm}$ and at the same time probing the energy, then the effect of misalignment will be expressed in the acoustic energy density. Doing this, the acoustic energy drops from its maximum value $5.36\,\text{Pa}$ at $y_0 = 0$ to $3.71\,\text{Pa}$, almost a drop of 30 %, see Fig. 8.4. It is hard to say what happens with the radiation force during this parametric sweep, however this can be visualized with an animation[1]. During the sweep the force nodal plane moves with the alignment of the transducer and gets narrower for $y_0 \to 0$, however the directions of the forces are the same and that is why a possible misalignment of the transducer does not play a role in the acoustophoresis, within an error of $\pm 0.5\,\text{mm}$.

[1] https://media.giphy.com/media/3ohzdVtE3Xkk01qFcQ/giphy.gif - follow link to see animation.

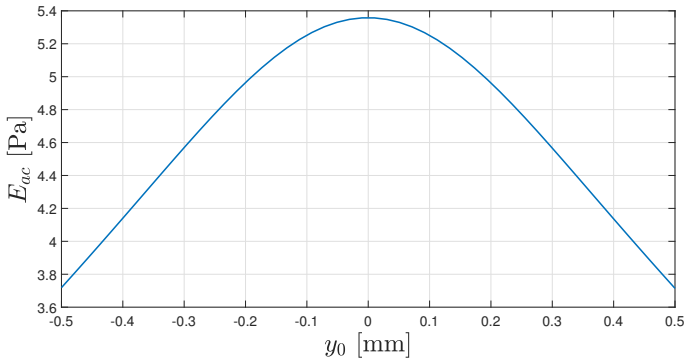

Figure 8.4: Line plot of the acoustic energy density as a function of the misalignment parameter y_0, using configuration B^{bot} actuated at 1.63 MHz. With 50 steps in y_0 equivalent to a step size of 0.02 mm.

8.3.2 Dimensional and mechanical parameters

The manufacturer of the devices stated an error of $\pm 15\,\mu\text{m}$ in the fluid channel dimensions, again this will have an impact on the resonances, since altering the dimensions of the device will yield a different resonating frequency.

Since there exists arbitrary many permutations of these error we only cover the extremes:

(i) Both dimensions having $+15\,\mu\text{m}$ in error.

(ii) Both dimensions having $-15\,\mu\text{m}$ in error.

(iii) The height H_F having $+15\,\mu\text{m}$ and the width W_F having $-15\,\mu\text{m}$.

(iv) The height H_F having $-15\,\mu\text{m}$ and the width W_F having $+15\,\mu\text{m}$.

(v) And also in between the four scenarios.

By introducing a parameter $\Delta = 15\,\mu\text{m}$ a parametric sweep can be computed. To analyze scenario (i) and (ii) the error is introduced as $H_F + \Delta$ and $W_F + \Delta$, in this way the sweep can be computed in the interval $\Delta = -15\,\mu\text{m}$ to $\Delta = +15\,\mu\text{m}$ covering both (i) and (ii) and also in between. For each step in Δ a solution is stored, and by choosing 50 steps corresponding to a step size of $0.6\,\mu\text{m}$, we get fifty solutions constructing an animation[2]. Evidently the effect is minute and the radiation force is almost the same during the sweep.

[2]https://media.giphy.com/media/xUPGcskDQiirYCz2uI/giphy.gif - follow link to see animation.

For the scenarios given in (iii) and (iv) we introduces the parameters as $H_F - \Delta$ and $W_F + \Delta$. Doing the same sweep as above will cover both (iii) and (iv) and also in between. Again the best way to illustrate the effects is to constitute an animation[3] and as it shows, almost nothing happens in the radiation force. Clearly the manufacturers tolerance are of no relevance in regards to the radiation force at resonance.

However the most influential parameters are Young's modulus E and Poisson's ratio ν, since both parameters are related to both the transverse c_T and longitudinal c_L speed of sound, actually both speeds are proportional to $\sqrt{E}$. As stated in table G.1 Young's modulus is given in the range from 2.4 GPa up to 3.3 GPa, where our analysis are conducted assuming that the PMMA is an average sample yielding a Young's modulus of 2.85 GPa. Assuming that there exists a relation between the eigenfrequencies f and the speed of sound like $c = f\lambda$, then

$$f \propto \sqrt{E}. \tag{8.7}$$

Allowing us to predict a translation in the frequency spectrum i.e. if instead we let $E = 3.3\,\text{GPa}$ then the frequency spectrum should be shifted by an amount $\sqrt{\frac{3.3}{2.85}} = 1.076$. This means that the eigenfrequency 1.63 MHz should be situated at 1.76 MHz when changing Young's modulus to 3.3 GPa. If instead we change it to $E = 2.4\,\text{GPa}$ the relative shift in frequency is $\sqrt{\frac{2.4}{2.85}} = 0.92$ i.e. the eigenfrequency should now be situated at 1.50 MHz. To compare this with the model, a frequency sweep is computed for all three values of Young's modulus. Fig. 8.5 shows that the spectrum remains almost the same but translated, the dashed lines indicates the theoretical predicted limits for the shifted frequencies and it seems to agree with the model. Even though a high uncertainty in Young's modulus yields a major effect in the frequencies, the spectrum remains the same but shifted.

[3] https://media.giphy.com/media/3ohzdFMSepzXg7DyRG/giphy.gif - follow link to see animation.

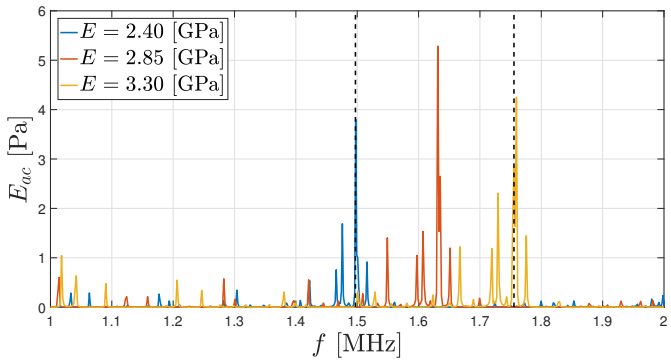

Figure 8.5: Line plot of the acoustic energy density as a function of frequency for device B actuated at the bottom, for different values of Young's modulus. The dashed lines indicates the predicted limits for the shift in the eigenfrequency 1.63 MHz, due to the change in Young's modulus for PMMA.

Poisson's ratio is also a major key in describing the solid, but the speed of sound is not proportional to this parameter and the simple analysis, as for Young's modulus, can not be represented for Poisson's ratio. To see the effect of the uncertainties in Poisson's ratio the model can be used to predict the upper and lower limit for which the eigenfrequencies belongs. As seen in Fig. 8.6 the change in spectrum seems to follow the same tendency as for the change in Young's modulus, however not as simple, but enough to give an upper and lower limit for which the eigenfrequency shifts.

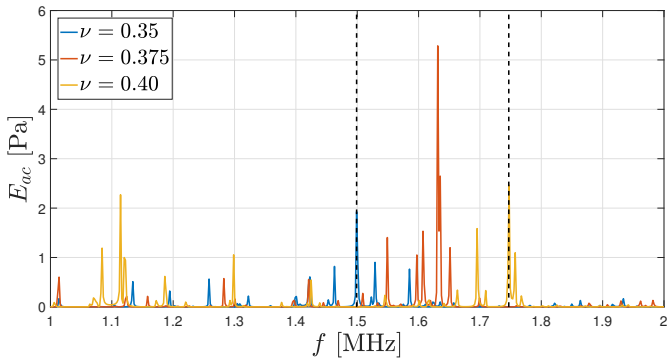

Figure 8.6: Line plot of the acoustic energy density as a function of frequency for device B actuated at the bottom, for different values of Poisson's ratio. The dashed line indicates the upper and lower limit for the shift in the eigenfrequency 1.63 MHz, due to the change in Poisson's ratio for PMMA. The lower limit is 1.499 MHz and the upper is 1.747 MHz.

8.4 Experimental results from AcouSort AB

We embarked on a field trip to Lund University in Sweden at 9th of July, to witness how the lab-research is conducted and the results from the fabricated devices (with dimensions specified in table G.3). The device we tested was corresponding to device D, but with a dimensions of $W_S = 3.00\,\text{mm}$ and $H_S + H_{lid} = 1.18\,\text{mm}$, where the discrepancy probably comes from the "hand-made" measurement with a vernier caliper. This bottom actuated Device D was tested with different flow rates and frequencies as seen in Fig. 8.7.

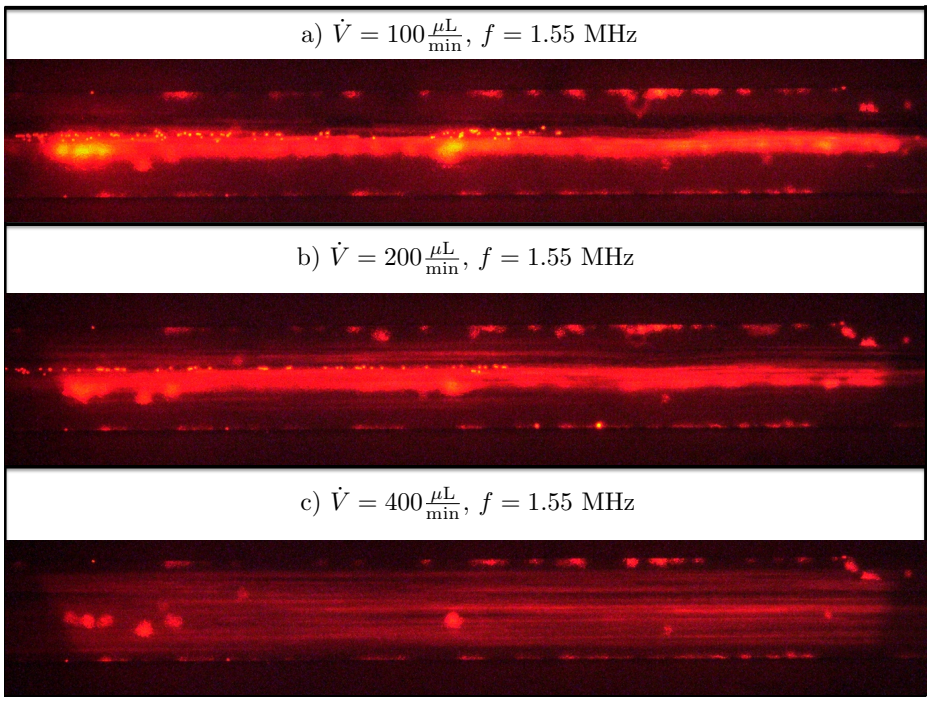

Figure 8.7: Top view of a particle focusing test in the laboratory bottom actuated Device D for different flow rates $\dot{V}$, with fluorescent particles of radius $a = 4.2\,\mu\text{m}(\pm 18\%)$[14] actuated asymmetrically (see fig. Fig. 7.1) at the same frequency $f = 1.55\,\text{MHz}$. a) shows the particle focusing effect at the lowest flow rate $\dot{V} = 100\,\mu\text{L}\,\text{min}^{-1}$, where it is also seen how the micro beads accumulate in two nodes (yellowish area). On picture b) the flow rate is increased to $\dot{V} = 200\,\mu\text{L}\,\text{min}^{-1}$, but still showing that the acoustic radiation force is able to keep particles focused mid-channel, whereas on c) the highest flow rate of $\dot{V} = 400\,\mu\text{L}\,\text{min}^{-1}$ is shown, and the particles are no longer focused. Note that some of the particle accumulation on the channel edges is originating from multiple use of same device.

It is seen how the the focusing of particles is dependant on the flow rate or flow velocity through the micro-channel. For the lowest flow rate $\dot{V}$ the acoustic radiation force F_{rad} is dominating, such that the micro beads are focused in the mid-channel (i.e. the zero pressure nodal plane) almost instantaneously. This effect is vanishing as the flow rate is increased, which can be seen on Fig. 8.7 b), where the focusing is happening a bit downstream. However, the effect of F_{rad} is still of a magnitude great enough to focus the particles, despite of the flow rate being twice as large compared to Fig. 8.7 a). It is also seen on Fig. 8.7 c) that when the flow rate once again is doubled to reach $\dot{V} = 400\,\mu\text{L}\,\text{min}^{-1}$ the radiation force is not strong enough to focus the micro beads effectively on the given length scale of approximately 40 mm. Nevertheless, if one looks very carefully, it can be seen that the beads begins to yield to the radiation force down the channel, by the thin line indicating focusing towards the end. Consequently, effectively focusing in such a device requires the radiation force, to be dominant relative to the flow rate on the device characteristic length scale. Therefore it is interesting to look at the time it takes for one particle to run through the channel. The velocity can be computed as,

$$v_x = \frac{\dot{V}}{A_F} = \frac{\dot{V}}{H_F W_F} = 29.63\,\text{mm}\,\text{s}^{-1} \quad \text{for} \quad \dot{V} = 200\,\mu\text{L}\,\text{min}^{-1}. \tag{8.8}$$

Which can be converted into the time it takes for one particle to travel through the entire channel of length $L_F = 40\,\text{mm}$ (seen on the schematic drawing Fig. G.1 and Fig. G.2) as

$$t = \frac{L_F}{v_x} = 1.35\,\text{s} \quad \text{for} \quad \dot{V} = 200\,\mu\text{L}\,\text{min}^{-1}. \tag{8.9}$$

where the flow rate of $\dot{V} = 200\,\mu\text{L}\,\text{min}^{-1}$ is chosen, since it is the highest flow rate still resulting in effective particle focusing which is desirable as it is less time consuming. When comparing to the particle simulations of the model, it was found that the critical flow rates for the two devices were $142\,\mu\text{L}\,\text{min}^{-1}$ for configuration B^{bot} and $270\,\mu\text{L}\,\text{min}^{-1}$ for configuration C^{top}, confirming that a higher force yields a higher value for the critical flow rate. Unfortunately, we obtained no measurements with steps small enough to precisely define an experimental value for the critical flow rate. Furthermore, the particle radius of $a = 4.2\,\mu\text{m}(\pm 18\%)$ is also a significant factor in comparison to our simulated results of particle focusing, as the radiation force scales with a^3 and the focusing times with a^2. Furthermore, it noteworthy that the critical radius of micro particles, making the radiation force dominant over acoustic streaming, is $a_c = 2\,\mu\text{m}$ [15], which fortuneately is a limit we are within.

It should also be noted that this experiment is one of several carried out on this

device. This have lead to accumulation of particles on the channel walls, which is partly obstructing the flow at certain points, thus given rise to unwanted effects. Since the solid material PMMA is highly sensitive to usual cleaning agents used in the laboratory as ethanol or similar of acidic nature, the only way to clean the device is by flushing, which have proved insufficient to the purpose. It is seen on Fig. 8.7 a) how the accumulation of beads to the left form a lump, giving the impression of poor focusing, which it not the case. This is also substantiated, as one can see stuck particles in the first part of the channel on Fig. 8.7 c) despite of the high flow rate, which may give rise to such uncertainties.

8.4.1 Experimental alignment

A video of the experimental results, also depicted in Fig. 8.7, was shot on our field-trip to Lund University and from this we were able to compute the time it takes to focus particles by video-analysis. The time it takes to focus particles of radius $a = 4.2\,\mu\text{m}$, from starting points near the channel-wall to their position approximately mid-channel of the candidate $D_{\text{exp}}^{\text{bot}}$ actuated at 1.55 MHz in the experiment was found to be $t = 1.2\,\text{s}$. By inserting this time, and assuming that all the same parameters apply in Eq. (8.3), the resulting energy was found to be $E_{ac} \approx 19\,\text{Pa}$.

Knowing that the experimental setup corresponds to a off-center transducer with $y_0 = 85\,\mu\text{m}$, by considering picture Fig. H.1 and fluorescent polystyrene particles with radius $a = 4.2\,\mu\text{m}$, with scattering coefficients $f_1 = 0.48$ and $f_2 = 0.052 - 0.003i$ [16].

However a simple calibration to the measured values can be made by scaling Young's modulus. At $f = 1.55\,\text{MHz}$ the measured radiation force is strongest, where the model yields $f = 1.4960\,\text{MHz}$, then the effective scaling of Young's modulus becomes $\tilde{E} = \left(\frac{1.55}{1.4960}\right)^2 = 1.073$. Effectively Young's modulus of the measured device becomes 3.06 GPa and the new eigenfrequency for the model becomes 1.548 MHz with the acoustics energy density 3.41 Pa.

Assuming that the acoustic energy density is proportional to the squared displacement, then by means of Eq. (4.18) we assume that $E_{ac} \propto d_0^2$, so

$$\frac{E_{ac}^{exp}}{E_{ac}} = \left(\frac{d_0^{exp}}{d_0}\right)^2 = \left(\frac{19.4\,\text{Pa}}{3.4\,\text{Pa}}\right)^2. \tag{8.10}$$

Evidently the actuation amplitude should be scaled with 2.4 yielding an amplitude of $d_0 = 0.24\,\text{nm}$.

The point of this analysis is to get a better feeling of what happens at the

transducer-solid interface and by all means it is much more complex. However by scaling the actuation amplitude with 2.4 yielding $d_0 = 2.4\,\mathrm{nm}$ we get results which is in the same order of magnitude than that of the measured.

Chapter 9

Concluding discussion

In this thesis we have conducted research on polymer-based acoustophoretic devices, coupling the elastic solid, fabricated in PMMA, with a micro channel containing water. The issue addressed in this thesis is the coupling of PMMA, a low acoustic impedance material, with water. Trying to find acoustic eigenmodes of such a system. At the moment such microfluidic devices is made of high acoustic impedance materials as silicon and glass and utilized for various purposes e.g. cell separation [17, 18]. These materials are generally more expensive and thus it is indeed desirable to produce such devices in polymers, since it is cost-efficient [19].

We have constructed a model from our theoretical studies, and implemented it in `COMSOL`. Our model of PMMA based devices coupled with water, has shown to be successful, when inducing a push-pull actuation at MHz frequencies. In section 6.3 we confirmed that the computed numerics and derived analytics are coherent with our model, for both the pressure (seen in Fig. 6.3) and displacement (seen in Fig. 6.5) and in Chapter 7 we showed that acoustofluidic PMMA-based devices are very different from harder elastic solids as silicon or glass.

With `COMSOL` simulations we did a candidate screening of the different geometrical devices proposed by `AcouSort`. The purpose of the screening was to find the best devices in terms of acoustophoresis, where displacement, pressure, acoustic energy density and forces were to be calculated and evaluated. Evidently the best acoustophoresis is obtained using the bottom-actuated device B and the top-actuated device D.

Furthermore we conducted particle tracking simulations (Fig. 8.3), to visualize and investigate the acoustophoretic effectiveness of the chosen candidates according to our model. It is seen on Fig. 8.1, how the force field is of top-actuated device C is less uniformly distributed in terms of force directions than the bottom-actuated

device B. Thus when we simulated the particle trajectories, it was found that ∼22% percent of the micro-beads escape due to this force field distribution. However, we did chose to select this candidate as it yielded the highest magnitude of radiation force of 315 pN resulting in particle focusing in just 0.5 s. For the bottom actuated Device B, a particle loss of ∼7% with a focusing time on 0.95 s due to a radiation force of 109 pN was shown.

Since high flow rates in such devices is wanted, these particle focusing times is translated into a critical flow rate, where the shorter time span of particle focusing of top actuated device C, results in a higher critical flow rate. Evidently, the two devices perform well on different parameters. It can be argued that for applications which need a high percentage of trapped particles, bottom actuated device B should be used and on the other hand, for applications where time-consuming investigations is a major issue, the top-actuated device C should be used. It comes down to the trade-off between time-efficient focusing of particles with a greater loss or vice versa. It should however be duly noted that the particle tracing simulations are carried out, such that once a particle touches the wall, it will get stuck at that position, whereas these particles in reality might be able to recover and afterwards get trapped.

Since the acoustic devices to be tested by `AcouSort`, will be actuated at the bottom as seen in Fig. 6.2, our comparisons can only be of devices actuated at the bottom. However, it is important to realize that the top-actuated devices in general yielded better results, than bottom-actuated devices in terms of acoustic force and energy magnitudes. Thus it is important to experimentally conduct research on these top-actuated devices to confirm this tendency. Furthermore, the only received experimental results was conducted on device D, which is not expected as being the best device candidate according to our analysis. Therefore it is indeed desirable to see how coherent the experimental results are compared to the predictions of our model.

We went to Lund University in Sweden the 9th of July, where we received our first experimental results, performed on bottom actuated device D, as depicted in Fig. 8.7, where acoustophoresis of 4.2 µm radius micro beads actuated at 1.55 MHz for different flow rates are shown. From video-analysis of this acoustophoresis, we found that the effective focusing time was 1.2 s, corresponding to an energy of magnitude 19 Pa. After receiving the experimental results, we were able to calibrate our model to the experimental parameters by scaling Young's modulus, such that the eigenfrequency matched the experimental. Afterwards a scaling in the actuation amplitude was made to match the estimated experimental energy, resulting in an actuation displacement magnitude of $d_0 = 0.24$ nm. In the parametric studies an amplitude of $d_0 = 0.1$ nm was used, which consequently suggests that our results generally will underestimate the acoustic energy and thus also radiation force.

9.1 Future perspectives

In the 2D model the flow is assumed to be invariant in the length direction, however this is not the case, since that the acoustophoretic speed through the entire channel length is non-homogeneously distributed [20]. Thus expanding our model to 3D is indeed necessary to obtain a higher accuracy for the results by including such 3D effects. This will however require much better hardware, if the error of the solutions should be of acceptable magnitudes as in Fig. 6.6. Henceforth, an interesting result appears from calibrating our model to experimental results, showing that the amplitude of displacement $d_0 = 0.24\,\text{nm}$ is yielding the experimentally estimated acoustic energy. Consequently, to model the acoustofluidic devices treated in this thesis by the analytic expression for the (push-pull) actuation, the displacement should be chosen accordingly.

The piezoelectric transducer is important in the sense that the acoustophoresis originates from the actuation induced by this. In this thesis the actuation is modelled as displacement in the solid, but introducing more sophisticated physics e.g. coupling electrodynamics with displacement will probably make the model more exact.

One effect which is present, but not included in our model is the acoustic streaming, which is a second-order effect. Including this would be preferable, however for particles with radius larger than $\sim 2\,\mu\text{m}$ the radiation force dominates and acoustic streaming can be neglected [15].

For future investigations, it would also be very interesting to compare new measurements on the acoustofluidic devices with our calibrated model, to see if this calibration is general applicable for other candidates as well, since parameters like Young's modulus varies a lot for different samples. It have been shown how to experimentally determine Young's modulus of polymers like PMMA by various methods [21, 22]. Thus experimental determination of the material parameters Young's modulus and/or Poisson's ratio for every unique sample would be optimal, since this would reduce the uncertainties in this parameter space and consequently yield more accurate results from the model. However, we realize that this would be a tiresome process, therefore we suggest to just perform determination of of Young's modulus and Poisson's ratio on a collection of devices, thus statistically reduce the interval of these material parameters. However, the uncertainties connected to these does not change the fact that acoustophoresis for soft elastic materials like PMMA is working.

Appendix A

Poisson distribution

The Poisson distribution

$$\Pr(n|N) = \frac{N^n}{n!}\exp(-N), \quad n \in \mathbb{N}_0 \tag{A.1}$$

describes the probability that an event happens n times in an interval with the average N events per interval. In our case N is the average number of molecules in V so the probability of finding n particles in V is given by Eq. (A.1). This distribution assumes

- Events are occuring independently
- The probability of an event is independent of time

said in other words, the events are occurring randomly and independently.

Appendix B

Mathematical formalism

B.1 Index notation

A neat way of formulating vectors and tensors is by index notation. A vector will have one index, corresponding to the running through each element of the vector, and a tensor will have to indices; first index corresponds to row and second to column. Consider the vector

$$\boldsymbol{x} = x_i = \begin{bmatrix} x_1 \\ x_2 \\ x_3 \\ \vdots \\ x_n \end{bmatrix} \tag{B.1}$$

for $i = 1, 2, 3, \ldots, n$. That is, the i'th component of that vector.

and the matrix

$$\boldsymbol{A} = A_{ij} = \begin{bmatrix} A_{11} & A_{12} & A_{13} & \ldots & A_{1n} \\ A_{21} & A_{22} & A_{23} & \ldots & A_{2n} \\ \vdots & \vdots & \vdots & \ddots & \vdots \\ A_{d1} & A_{d2} & A_{d3} & \ldots & A_{dn} \end{bmatrix} \tag{B.2}$$

for $i = 1, 2, 3, \ldots, d$ and $j = 1, 2, 3, \ldots, n$.

Hence by means of the the above, the index notation of gradients and divergences

vector calculus, becomes

$$\boldsymbol{\nabla} \cdot \boldsymbol{x} = \partial_i x_i, \tag{B.3a}$$
$$\boldsymbol{\nabla} \boldsymbol{x} = \partial_j x_i, \tag{B.3b}$$
$$\boldsymbol{\nabla} \cdot \boldsymbol{A} = \partial_j A_{ij}. \tag{B.3c}$$

Using Einstein summation convention

$$\boldsymbol{x} = \begin{bmatrix} x_1 \\ x_2 \\ x_3 \\ \vdots \\ x_n \end{bmatrix} = \sum_i^n x_i \hat{e}_i = x_i \hat{e}_i \tag{B.4}$$

where the repeated index implies summation over the index. For cartesians vector $i = x, y, z$. The unit tensor in indexnotation

$$\mathbf{1} = \delta_{ij} \tag{B.5}$$

B.2 Derivatives

Derivatives in this thesis are denoted as follows:
For ordinary derivatives

$$\frac{\mathrm{d}x}{\mathrm{d}t} = \mathrm{d}_t x \tag{B.6}$$

and for partial derivatives

$$\frac{\partial x}{\partial t} = \partial_t x \tag{B.7}$$

B.3 Identities and theorems

Gauss' theorem

If $\boldsymbol{J}$ is a continuously differentiable vector field defined on a neighborhood of Ω, then

$$\int_\Omega \boldsymbol{\nabla} \cdot \boldsymbol{J} \, \mathrm{d}V = \oint_{\partial\Omega} \boldsymbol{J} \cdot \boldsymbol{n} \, \mathrm{d}A \tag{B.8}$$

where $\partial\Omega$ is the closure of Ω.

Green's first identity

$$\int_\Omega (g\boldsymbol{\nabla}\cdot\boldsymbol{J} + \boldsymbol{J}\cdot\boldsymbol{\nabla}g) = \oint_{\partial\Omega} g(\boldsymbol{J}\cdot\boldsymbol{n})\mathrm{d}A \tag{B.9}$$

B.4 Reynold's transport theorem

As in Eq. (1.6) where we considered the rate of change in local values (intrinsic) we will now look at the rate of change in global values. Considering the time interval $t+\Delta t$ we can write the change in volume as $\Omega(t+\Delta t) = \Omega(t)+\Delta\Omega$, leaving Eq. (1.8) as

$$\begin{aligned}\frac{\mathrm{d}G(t)}{\mathrm{d}t} &= \frac{\mathrm{d}}{\mathrm{d}t}\int_{\Omega(t)} J(\boldsymbol{r},t)\,\mathrm{d}V \\ &= \lim_{\Delta t\to 0}\left[\frac{\int_{\Omega(t+\Delta t)} J(\boldsymbol{r},t+\Delta t)\,\mathrm{d}V - \int_{\Omega(t)} J(\boldsymbol{r},t)\,\mathrm{d}V}{\Delta t}\right],\end{aligned} \tag{B.10}$$

where $J(\boldsymbol{r},t) = g(\boldsymbol{r},t)\rho(\boldsymbol{r},t)$. Rewriting Eq. (B.10) knowing that $\Omega(t+\Delta t) = \Omega(t)+\Delta\Omega$,

$$\begin{aligned}\frac{\mathrm{d}G(t)}{\mathrm{d}t} &= \lim_{\Delta t\to 0}\left[\frac{\int_{\Omega(t)} J(\boldsymbol{r},t+\Delta t) - J(\boldsymbol{r},t)\,\mathrm{d}V + \int_{\Delta\Omega} J(\boldsymbol{r},t)\,\mathrm{d}V}{\Delta t}\right] \\ &= \lim_{\Delta t\to 0}\left[\int_{\Omega(t)} \frac{J(\boldsymbol{r},t+\Delta t) - J(\boldsymbol{r},t)}{\Delta t}\,\mathrm{d}V\right] + \lim_{\Delta t\to 0}\left[\int_{\Delta\Omega}\frac{J(\boldsymbol{r},t)}{\Delta t}\,\mathrm{d}V\right].\end{aligned} \tag{B.11}$$

In the time Δt the surface element $\mathrm{d}A$, with velocity $\boldsymbol{v}_s$, has swept out a volume $\mathrm{d}V = \Delta t\boldsymbol{v}_s\cdot\boldsymbol{n}\,\mathrm{d}A$, corresponding to a volume element in $\Delta\Omega$. Writing the volume integral over $\Delta\Omega$ as a surface integral over $\partial\Omega$ and letting $\Delta t \to 0$ Eq. (B.11) becomes

$$\frac{\mathrm{d}G(t)}{\mathrm{d}t} = \int_{\Omega(t)} \frac{\partial J(\boldsymbol{r},t)}{\partial t}\,\mathrm{d}V + \oint_{\partial\Omega} J(\boldsymbol{r},t)\boldsymbol{v}_s\cdot\boldsymbol{n}\,\mathrm{d}A, \tag{B.12}$$

also known as the Reynolds transport theorem. Again $J(\boldsymbol{r},t)$ is a tensor field.

Appendix C

COMSOL syntax and implementation

To elaborate on the implementation of the model given in section 6.2, please appreciate this appendix. COMSOL syntax

$$p = \texttt{p} \tag{C.1a}$$
$$\boldsymbol{u} = \texttt{(uY,uZ)} \tag{C.1b}$$
$$\boldsymbol{F}_s = \texttt{(fsY,fsZ)} \tag{C.1c}$$
$$F_f = \texttt{fF} \tag{C.1d}$$
$$(\boldsymbol{\sigma})_{ij} = \texttt{ssij} \tag{C.1e}$$

The governing equations are implemented under the weak-form PDE module

$$\boldsymbol{\nabla}\cdot\boldsymbol{\nabla}p + F_f = 0 \left\{ \quad \texttt{-(test(py)*py+test(pz)*pz) + test(p)*fF} \right. \tag{C.2a}$$

$$\boldsymbol{\nabla}\cdot\boldsymbol{\sigma} + \boldsymbol{F}_s \;\; = \boldsymbol{0} \left\{ \begin{array}{l} \texttt{-(test(uYy)*smYY+test(uYz)*smYZ)+test(uY)*fsY} \\ \texttt{-(test(uZy)*smZY+test(uZz)*smZZ)+test(uZ)*fsZ:} \end{array} \right. \tag{C.2b}$$

implemented as

The boundary conditions

$$\text{solid-air :} \qquad \boldsymbol{\sigma}_s\cdot\boldsymbol{n} = \boldsymbol{0} \qquad \texttt{No flux} \tag{C.3a}$$
$$\text{solid-transducer :} \qquad \boldsymbol{u} = d(y)\hat{\boldsymbol{e}}_z \qquad \texttt{Constraint} \tag{C.3b}$$
$$\text{solid-fluid :} \qquad \boldsymbol{\sigma}_s\cdot\boldsymbol{n} = -p\boldsymbol{n} \qquad \texttt{Weak contribution} \tag{C.3c}$$
$$\text{fluid-solid :} \qquad \boldsymbol{n}\cdot\boldsymbol{\nabla}p = \rho_f\omega^2\boldsymbol{n}\cdot\boldsymbol{u} \qquad \texttt{Weak contribution} \tag{C.3d}$$

Implementation of Eq. (C.3c):

```
test(uY)*(-p*ny) + test(uZ)*(-p*nz);
```
(C.4)

and Eq. (C.3d)

```
test(p)*(rhof*omega^2*(ny*uY+nz*uZ))
```
(C.5)

Appendix D

Lorentzian shaped function

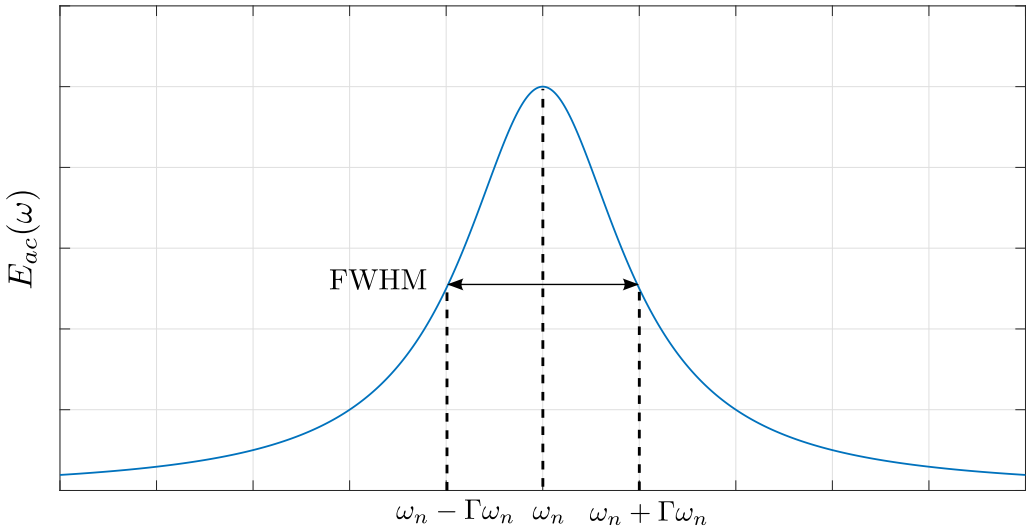

Figure D.1: Energy density as a function of angular frequency around the resonance ω_n, illustrating the Lorentzian lineshape, where the damping coefficient Γ determines the width.

Appendix E

Diverging and change in volume

By utilizing the symmetric nature of the strain tensor Eq. (5.5) it can be diagonalized in any local coordinate system, by the three vectors constituting an orthonormal basis, described as

$$\boldsymbol{s} = \lambda^{(1)}\hat{\boldsymbol{e}}_1 \cdot \hat{\boldsymbol{e}}_1^{\intercal} + \lambda^{(2)}\hat{\boldsymbol{e}}_2 \cdot \hat{\boldsymbol{e}}_2^{\intercal} + \lambda^{(3)}\hat{\boldsymbol{e}}_3 \cdot \hat{\boldsymbol{e}}_3^{\intercal} \tag{E.1}$$

it can be shown from three linearly independent and infinitesimal needles spanning a parallelepiped, that the volume of this changes due to displacement as

$$\boldsymbol{\nabla} \cdot \boldsymbol{u} = \frac{\delta(\mathrm{d}V)}{\mathrm{d}V} \tag{E.2}$$

which consequently shows that the divergence of displacement is to be appreciated as the local relative change of volume.

Appendix F

Convergence analysis - supplements

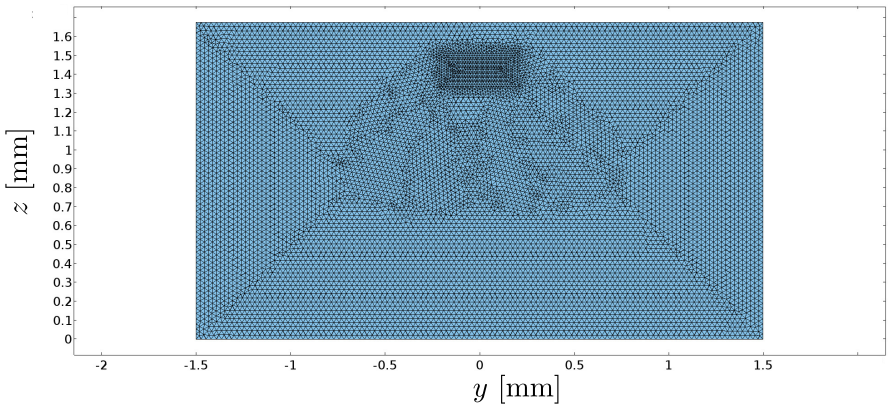

Figure F.1: Mesh consisting of a total 19194 elements in the fluid and solid domain. The coarseness of this mesh corresponds to the value for the pressure field $C_p \approx 0.35$ or an error of $\approx 35\%$ and value of the displacement field $C_u \approx 0.21$ or an error of $\approx 21\%$.

Appendix G

Material and dimensional parameters

All material parameters are given at 25 °C

	Silicon	PMMA	Pyrex 7740 [23]
Density ρ [kg/m^3]	2329	1190 [24]	2230
Young's modulus E [GPa]	169 [25]	2.85 (2.4-3.3) [26]	62.75
Poisson's ratio ν	0.064 [25]	0.375 (0.35-0.40) [26]	0.20
Speed of sound (transverse) c_T [m/s]	5845 [27]	933.2	3424
Speed of sound (longitudinal) c_T [m/s]	8433 [27]	2086	5592
Effective damping [3] Γ	0.0004	0.0004	0.0004

Table G.1: Parameters used to model both Silicon, PMMA and Pyrex.

Material	Density ρ [kg/m^3]	Speed of sound c [m/s]	Effective damping Γ	Dynamic viscosity η [mPa s]	β
Water [28]	997.05	1496.7	0.004 [3]	0.890	3

Table G.2: Parameters used to model water

Device	H_S [mm]	H_{lid} [mm]	W_S [mm]	W_F [mm]	H_F [mm]	L_S [mm]	L_F [mm]
A	1.50	0.175	3.00	0.375	0.150	50	40
B	1.50	0.175	5.00	0.375	0.150	50	40
C	1.00	0.175	5.00	0.375	0.150	50	40
D	1.00	0.175	3.00	0.375	0.150	50	40

Table G.3: Dimensions of the different PMMA devices, used by `AcouSort`.

G.1 Parameters used in COMSOL

Name	Expression/Value	Units	Description
a	10	[um]	particle radius
β	3		beta value for water
c_0	1496.7	[m/s]	Speed of sound (water)
c_L	Eq. (5.26)		Longitudinal speed of sound (isotropic)
c_L^{Si}	8433	[m/s]	Si Speed of sound, (Silicon)
c_T	Eq. (5.26)		Transverse speed of sound (isoptropic)
c_T^{Si}	5845	[m/s]	PMMA Speed of sound, (Silicon)
d_0	0.1	[nm]	actuator amplitude
d_y	0.05*WS		Finite gap between push-pull transducer
E^{PMMA}	2.85	[GPa]	Youngs PMMA
E^{Si}	169	[GPa]	Youngs modulus of silicon (WIKI)
η	8.90E-04	[Pa*s]	Dynamic viscosity (water)
f	sweep	[MHz]	test freq.
f_1	Eq. (4.24)		inviscous monopole coefficiet
f_1^{ps}	0.48		monopole coef. polystyrene
f_2	Eq. (4.24)		inviscous dipole coefficient
f_2^{ps}	0.052-0.003*i		dipole coef. polystyrene
g	9.815	[m/sˆ2]	Gravitational acceleration
Γ_f	0.004		Damping coefficient (solid)
Γ_s	0.0004		Damping coefficient (water9
H_F	0.15	[mm]	Fluid channel width
hFluid	0.5*hSize		Fluid mesh
H_S	1.5	[mm]	Solid height
H_{lid}	0.175	[mm]	Layer height
hSize	0.05*HS		Element scale
hSolid	1*hSize		Solid mesh
κ_f	1/(rhoF*cFˆ2)		Compressibility (water)
ν^{PMMA}	0.375		Poisson PMMA
ν^{Si}	0.064		Poissons ratio (WIKI)
ω	2*pi*f		Ang. freq.
ρ^{PMMA}	1190	[kg/mˆ3]	PMMA density
ρ^{Si}	2329	[kg/mˆ3]	Mass density silicon (S denoting solid prop.)
ρ_f	997.05	[kg/mˆ3]	Mass density (water)
ρ_P	1050	[kg/mˆ3]	Particle density
W_F	0.375[mm]		Fluid channel height
W_S	5	[mm]	Solid width

Table G.4: Parameters used for COMSOL modelling, with given values/expressions, units and description.

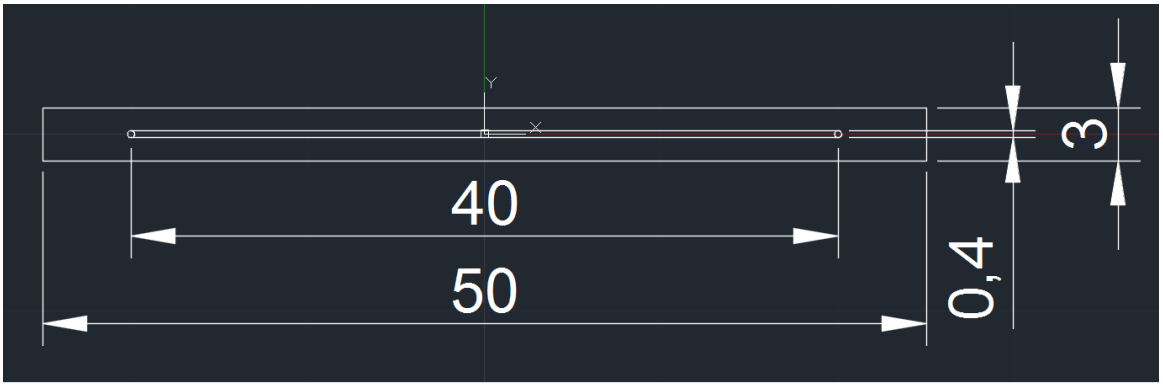

Figure G.1: Top down view schematics of device A and B, units given in mm.

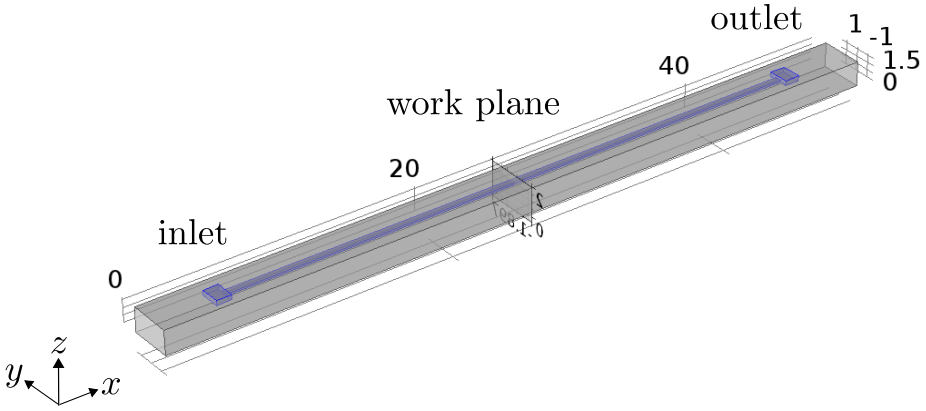

Figure G.2: 3D schematics of device A, units given in mm.

Appendix H

Parametric studies

H.1 Experimental setup

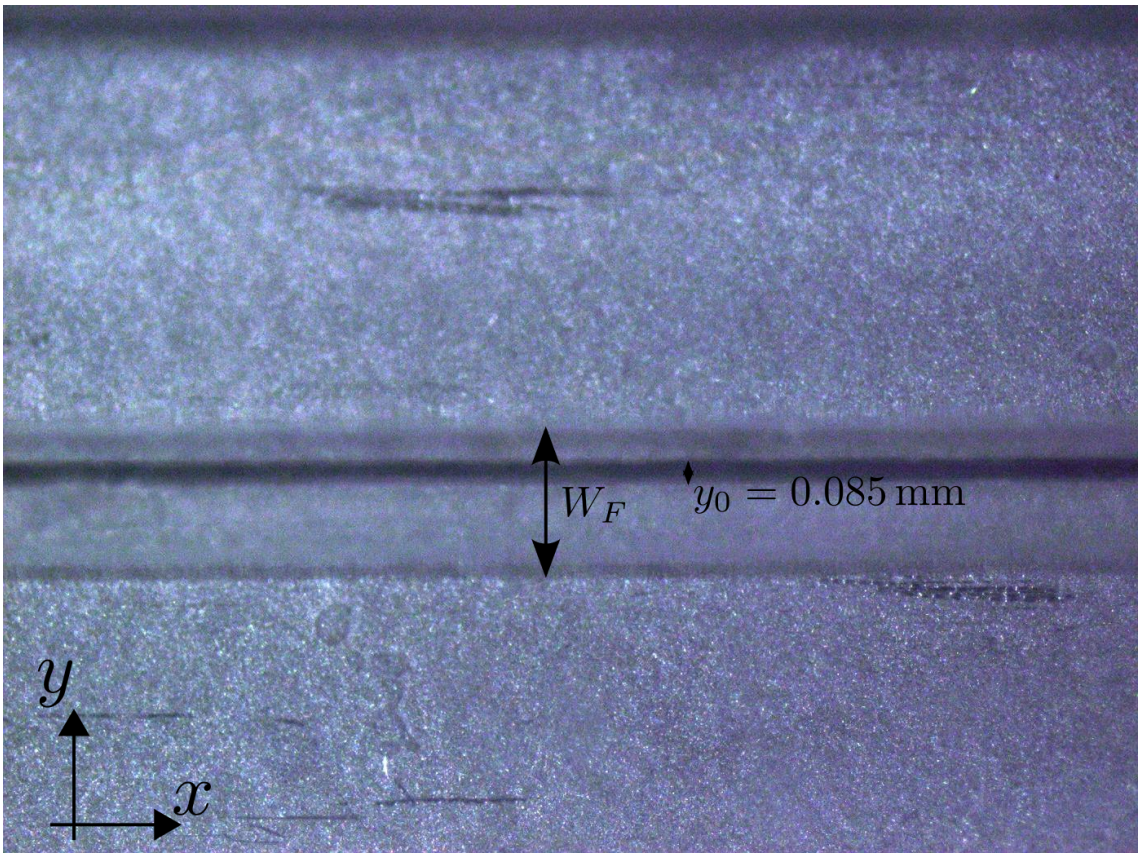

Figure H.1: Picture of the PMMA device seen from above with the carved transducer in the middle (black line with width y_0).

H.2 Bottom-actuation of devices

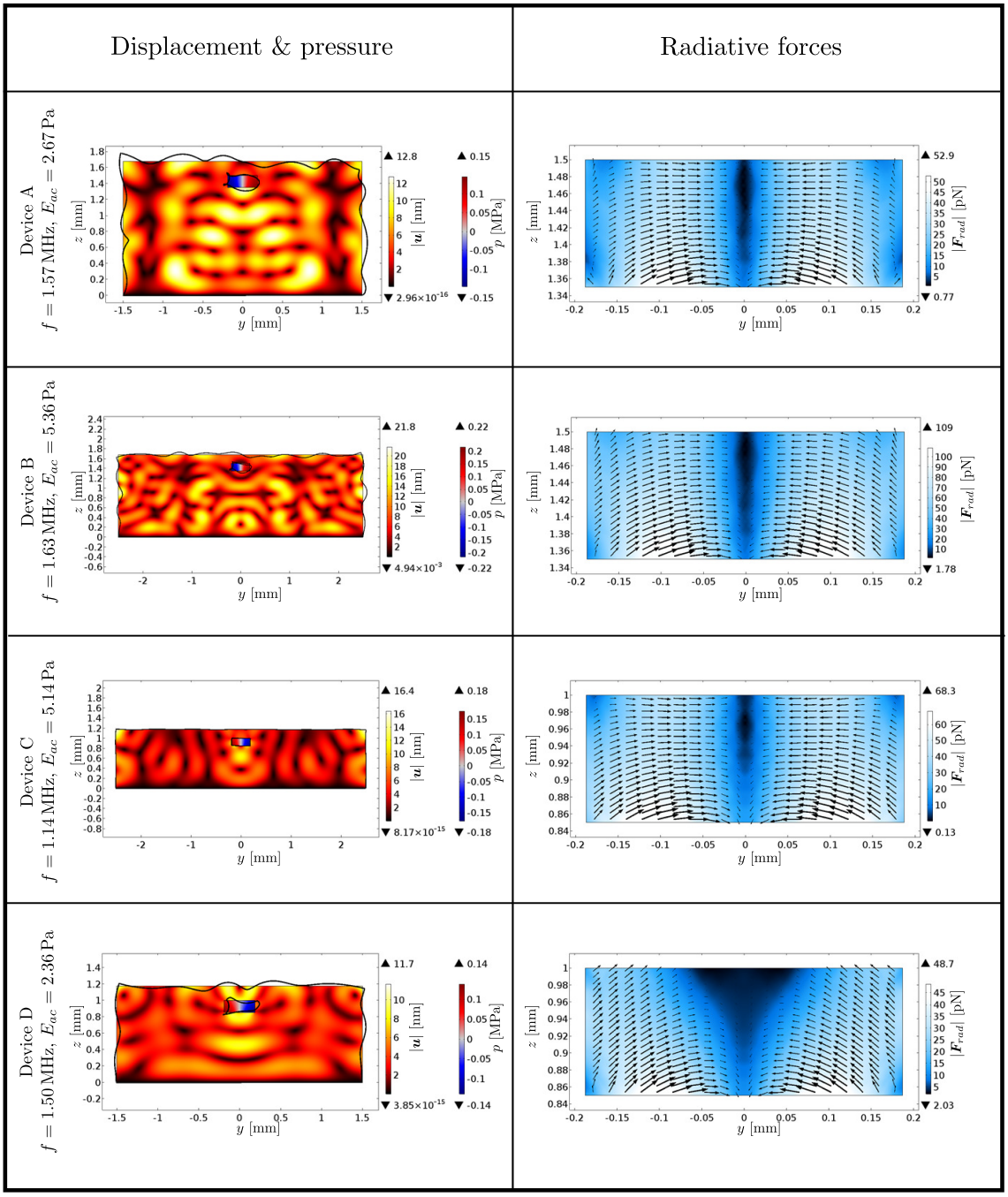

Figure H.2: The best eigenfrequencies and their associated displacement, pressure and force fields. The actuated frequency and acoustic energy density is noted for each device. The used scattering coefficients are $f_1 = 0.44386$ and $f_2 = 0.034194$ and particles with radius $a = 10\,\mu\mathrm{m}$.

H.3 Top-actuation of devices

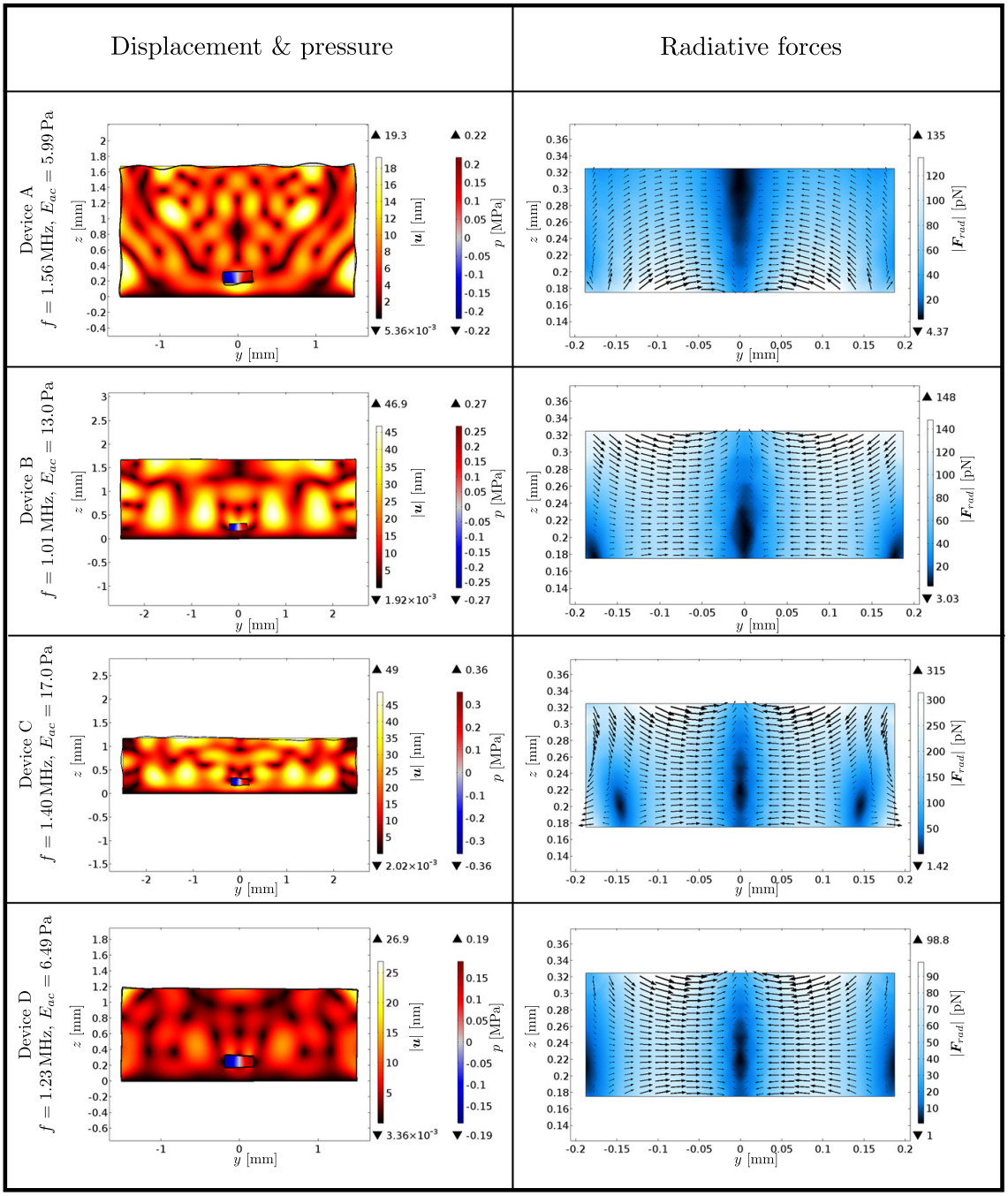

Figure H.3: The best eigenfrequencies and their associated displacement, pressure and force fields. The actuated frequency and acoustic energy density is noted for each device. The used scattering coefficients are $f_1 = 0.44386$ and $f_2 = 0.034194$ and particles with radius $a = 10\,\mu\mathrm{m}$.

References

[1] H. Bruus, "Acoustic streaming," `http://www.staff.dtu.dk/bruus` (2016), note, DTU.

[2] S. J. Blundell and K. M. Blundell, *Concepts in Thermal Physics*, 2nd ed. (Oxford University Press, Oxford, 2009).

[3] P. Hahn and J. Dual, "A numerically efficient damping model for acoustic resonances in microfluidic cavities," Physics of Fluids **27** (2015), 10.1063/1.4922986.

[4] M. Settnes and H. Bruus, "Forces acting on a small particle in an acoustical field in a viscous fluid," Physical Review E **85**, 1–12 (2012), 10.1103/PhysRevE.85.016327.

[5] B. Lautrup, *Physics of Continuous Matter*, 2nd ed. (CRC Press, Boca Raton, 2011).

[6] H. Bruus, "An introduction to the theory of acoustic waves in elastic solids," `http://www.staff.dtu.dk/bruus` (2016), lecture notes, DTU.

[7] Comsol, "Multiphysics Simulation Software - Platform for Physics-Based Modeling," (2017), https://www.comsol.dk/comsol-multiphysics.

[8] H. Bruus, "Implementation of first- and second-order acoustic perturbation theory in Comsol," `http://www.staff.dtu.dk/bruus` (2016), note, DTU.

[9] H. Bruus, "Fluid-solid coupling in COMSOL," `http://www.staff.dtu.dk/bruus` (2017), note, DTU.

[10] H. Bruus, "Microfluidic streaming induced by an oscillating microscope glass slide," `http://www.staff.dtu.dk/bruus` (2014), note, DTU.

[11] L. D. Landau and E. M. Lifshitz, *Theory of Elasticity. Course of Theoretical Physics.*, 3rd ed. (Pergamon Press, Oxford, 1986).

[12] R. P. Moiseyenko and H. Bruus, "Mixed shear and longitudinal ultrasound wave resonances in polymer chips enabling microchannel acoustophoresis," unpublished preprint , 1–8 (2017), dTU.

[13] R. Barnkob, P. Augustsson, T. Laurell, and H. Bruus, "Measuring the local pressure amplitude in microchannel acoustophoresis," Lab on a Chip **10**, 1473–197 (2010), 10.1039/b920376a.

[14] O. Jakobsson, "Private communication," (2017).

[15] P. M. Tribler, *Acoustic streaming in microchannels - The trinity of analytics, numerics and experiments*, PhD, DTU (2015), http://web-files.ait.dtu.dk/bruus/TMF/publications/PhD/PhD_2015_PBM.pdf.

[16] P. B. Muller, R. Barnkob, M. J. H. Jensen, and H. Bruus, "A numerical study of microparticle acoustophoresis driven by acoustic radiation forces and streaming-induced drag forces," Lab on a Chip **12**, 4617 (2012), 10.1039/c2lc40612h.

[17] F. Petersson, L. Åberg, A.-M. Swärd-Nilsson, and T. Laurell, "Free flow acoustophoresis: Microfluidic-based mode of particle and cell separation," Analytical Chemistry **79**, 5117–5123 (2007), 10.1021/ac070444e.

[18] J. Shi, X. Mao, D. Ahmed, A. Colletti, and T. J. Huang, "Focusing microparticles in a microfluidic channel with standing surface acoustic waves SSAW," Lab Chip **8**, 221–223 (2008), 10.1039/B716321E.

[19] A. Mueller, A. Lever, T. V. Nguyen, J. Comolli, and J. Fiering, "Continuous acoustic separation in a thermoplastic microchannel," Journal of Micromechanics and Microengineering **23** (2013), 10.1088/0960-1317/23/12/125006.

[20] P. Augustsson, R. Barnkob, S. T. Wereley, H. Bruus, and T. Laurell, "Automated and temperature-controlled micro-PIV measurements enabling long-term-stable microchannel acoustophoresis characterization," Lab on a Chip **24** (2011), 10.1039/c1lc20637k.

[21] D. Tranchida and S. Piccarolo, "On the Use of the Nanoindentation Unloading Curve to Measure the Young's Modulus of Polymers on a Nanometer Scale," Macromolecular Rapid Communications **26**, 1800–1804 (2005), 10.1002/marc.200500538.

[22] C. Reynaud, F. Sommer, C. Quet, N. El Bounia, and T. M. Duc, "Quantitative determination of Young's modulus on a biphase polymer system using atomic force microscopy," Surface and Interface Analysis **30**, 185–189 (2000).

[23] CORNING, *Glass Silicon Constraint Substrates*, Tech. Rep. (Corning, Houghton Park C-8, NY 14831, 1999).

[24] J. Van Deventer, T. Löfqvist, and J. Delsing, "PSpice simulation of ultrasonic systems," IEEE Transactions on Ultrasonics, Ferroelectrics, and Frequency Control **47**, 1014–1024 (2000).

[25] M. a. Hopcroft, W. D. Nix, and T. W. Kenny, "What is the Young ' s Modulus of Silicon ?" Journal of Microelctromechanical Systems **19**, 229–238 (2010), 10.1109/JMEMS.2009.2039697.

[26] GoodFellow, "Polymethylmethacrylate - Material Information," (2017), http://www.goodfellow.com/E/Polymethylmethacrylate.html.

[27] O. Madelung, U. Rössler, and M. Schulz, "Silicon (Si), sound velocities," in *Group IV Elements, IV-IV and III-V Compounds. Part b - Electronic, Transport, Optical and Other Properties* (Springer-Verlag, Berlin/Heidelberg, 2002) pp. 1–5, 10.1007/10832182_448.

[28] P. B. Muller and H. Bruus, "Numerical study of thermoviscous effects in ultrasound-induced acoustic streaming in microchannels," Physical Review E **90** (2014), 10.1103/PhysRevE.90.043016.